Structural investigation and sonophotocatalytic properties of the solid solutions $Sr(Mo_{1-x}W_x)O_4$ crystals synthesized by the sonochemical method

P. B. de Sousa[1], I. C. Nogueira[2], G. O. M. Gusmão[3], S. B.S. Gusmão[1], F. H.P. Lopes[3], B. S. Sousa[3], J. C. Sczancoski[4], A. F. Gouveia[5], and L. S. Cavalcante[1,3,*]

[1] *Programa de Pós-Graduação em Ciência e Engenharia dos Materiais–PPGCEM, Universidade Federal do Piauí, Teresina, PI 64049-550, Brazil*

[2] *Universidade Federal do Amazonas, ICE, P.O. Box 670, Av. Rodrigo Otávio, 4050, Japiim, Manaus, AM 69077-000, Brazil*

[3] *Universidade Estadual do Piauí, GERATEC–CETEM–PPGQ, Rua: João Cabral, N. 2231, P.O. Box 381, 64002-150 Teresina, PI, Brazil*

[4] *Universidade Estadual de Ponta Grossa-UEPG-Departamento de Física, Ponta Grossa, PR 84030-900, Brazil*

[5] *Department of Physical and Analytical Chemistry, Universitat Jaume I (UJI), Castellón de la Plana 12071, Spain*

ABSTRACT

In this paper, the solid solutions of strontium molybdate-tungstate [$Sr(Mo_{1-x}W_x)O_4$] crystals with ($x = 0$, 0.25, 0.50, 0.75, and 1) were synthesized by the sonochemical method. Their structure, morphology, optical, and sonophotocatalytic properties were performed in function of the replacement of Mo^{6+} by W^{6+} cations into the lattice. Their structure and elemental composition were characterized using X-ray diffraction, Rietveld refinement, micro-Raman, energy-dispersive X-ray, and Fourier-transform infrared spectroscopies proving that all samples are monophasic, crystalline, and exhibit a scheelite-type tetragonal structure. Field-emission scanning electron microscopy images revealed the octahedral and dumbbell-like morphologies for $SrMoO_4$ and $SrWO_4$ crystals. Moreover, it is noted to pass through spindle-like morphology for the microcrystals containing both Mo^{6+} and W^{6+} cations ($x = 0.25$, 0.50, and 0.75). Ultraviolet-visible diffuse reflectance spectroscopy showed a directly proportional increase in the optical band gap (E_{gap}) values from 4.27 to 5.01 eV. These data indicate an increase in the intermediary electronic levels between valance and conduction bands with the increase in the concentration of W^{6+} cations in the lattice. Finally, we have obtained good sonophotocatalytic performances for $SrMoO_4$ crystals (90%), and mainly to $Sr(Mo_{0.25}W_{0.75})O_4$ crystals (98%) in the degradation of Rhodamine B dye until 240 min under UV-C light.

Address correspondence to E-mail: laeciosc@gmail.com

🍿 Springer

	Journal : **10854 - Large 10854**	Dispatch : **17-9-2022**	Pages : **26**
	Article No. : **8985**	☐ LE	☐ TYPESET
	MS Code : **JMSE-D-22-02640R1**	☑ CP	☑ DISK

1 Introduction

Recently, molybdenum and tungsten oxides have been widely investigated due to their excellent chemical, physical, electronic, and structural properties [1]. Among them, alkaline earth metals, with the general formula ABO_4, have shown promise, offering several application opportunities aimed at different areas, such as electrochemical sensors, humidity sensors, scintillators, optical fibers, electrocatalysts, photocatalysts, capacitors, solar cells, microwave dielectric devices, light-emitting diodes, solid-state lasers, Raman lasers, electrodes for lithium-ion batteries, drug releases, and many others [2–8].

The electronic structure of the molybdates and tungstates can be changed with the size of divalent cation (A^{2+}) and can exhibit a scheelite-type tetragonal structure or wolframite-type monoclinic structure. In the scheelite structure ($r_A^{2+} > 1.0 \text{ Å}$, $A = \text{Ca, Sr, Ba, and Pb}$), the A^{2+} cations are coordinated with eight oxygen atoms, assuming a $[AO_8]$ deltahedral configuration, while the B^{6+} cations related to tungsten (W^{6+}) and/or molybdenum (Mo^{6+}) are surrounded by four equivalent O atoms, displaying a $[WO_4]$ or $[MoO_4]$ tetrahedral coordination. In the wolframite structure ($r_A^{2+} < 1.0 \text{ Å}$, $A = \text{Mg}$), both the A^{2+} and the W^{6+} or Mo^{6+} cations are coordinated by six O atoms [1, 9]. The scheelite structure is characterized by the space group $I4_1/a$ (No. 88) with four units of molecular formula per unit cell ($Z = 4$), in which the deltahedral and tetrahedral clusters are then slightly distorted [5, 10]. Several types of electronic or surface defects are associated with the structural order-disorder degree, such as oxygen vacancies and intermediate energy levels, giving these materials the ability to emit blue and green light under ultraviolet (UV)-excitation [9, 11, 12]. Therefore, these oxide materials have been widely applied as a host material for lanthanide ions. When doped, they transfer the absorbed energy to the doping ions, expanding the luminescent spectrum and application possibilities [13, 14].

It is well known that the physical, chemical, and structural properties of these oxide materials are depended of obtention methods [15, 16]. Until now, several synthesis methods have been developed, such as solid-state synthesis, co-precipitation, sol–gel, hydrothermal, solvothermal, electrochemical, sonochemical, polymeric precursor method, by ion injection, microwave [12, 17, 18]. Among the methods mentioned, the sonochemical method emerged as a powerful technique capable of promoting a variety of chemical reactions with savings of time and energy [19]. These beneficial points make the ultrasound equipment used in the sonochemical synthesis of oxide materials a technique of fast processing, very simple, low maintenance cost, and environmentally friendly as it uses water (H_2O) as a solvent in most chemical reactions. In addition to enabling large-scale production of different materials with a high degree of crystallinity and purity, with size and morphology control, without the need for high temperature or pressure, using low-cost equipment [20–22]. The fast processing is due to the effects arising from the phenomenon of acoustic cavitation [23].

According to the literature [24, 25], when aqueous suspensions are subjected to ultrasonic waves, vapor bubbles are generated in the liquid medium that constantly grows and implodes, producing microscopically located hot spots with temperatures that can exceed 5000 K, pressures above 1000 atm, and heating/cooling rates close to 10^{10} K s^{-1}. The extreme conditions of temperature and pressure created followed by a very fast cooling rate can be favorable for a wide range of chemical reactions [16, 26]. The shock waves created during the implosive collapse of the cavitation bubbles generate a strong turbulent flow in the liquid, improving mass transport, and causing a considerable increase in the speed of reactions. Furthermore, suspended solid particles can be accelerated by increasing inter-particle collision rates directly influencing their size, morphology, distribution, and surface composition [27, 28]. During the cavitation process, the large amount of energy released forms hydroxyl radicals (HO·) and reactive hydrogen (H·) by sonolysis of H_2O molecules [29]. Therefore, the sonochemical method has also been applied as one of the advanced oxidative methods for removal of organic pollutants from residual waters [30].

The degradation of organic pollutants by means of sonophotocatalysis occurs due to joint of ultrasound effect with active heterogeneous catalysts and a light source [31]. In the sonophotocatalytic process, it is possible to use both UV- and/or Visible(Vis)-lights to provide energy and stimulate the photocatalyst to generate electron↔hole (e^-↔h^+) pairs and produce more reactive species, ultrasound can also through sonoluminescence phenomenon. Additionally, the photocatalysts can act as an additional nucleus to form more cavitation bubbles [32, 33]. On the other

hand, the successive implosions of cavitation bubbles contribute to the continuous cleaning of the catalyst surface (regenerating its active sites) and prevent the agglomeration of particles, thus increasing the accessible surface area for the successive reactions mentioned above that lead to degradation of organic pollutants [34, 35].

Moreover, the strontium molybdates and tungstates ($SrMoO_4$ and $SrWO_4$) are considered to be promising photocatalysts for the degradation of many organic pollutants [36, 37] because they are low-cost materials with a diversity of syntheses, improved thermal and chemical stability, and attractive electrical, magnetic, and optical properties [3, 10, 12]. Among these organic pollutants are the dyes commonly present in industrial residual waters sometimes discharged into the aquatic environment without proper treatment, causing severe harm to its ecosystem and directly affecting humans, flora, fauna, and health due to the carcinogenic, genotoxic, and mutagenic nature of most of these dyes. Therefore, studies aimed at the complete degradation of these pollutants are of extreme importance and emergency [38, 39].

Previously, the authors focused their attention on the investigation of the structural, morphological, optical, and sonophotocatalytic (SPC) properties of calcium and strontium tungstate ($Ca_{1-x}Sr_x)WO_4$) with ($x = 0$; 0.25; 0.50; 0.75; and 1) synthesized by the sonochemical method, evaluating the influence of the gradual replacement of Ca^{2+} by Sr^{2+} cations on such properties [40]. As a way of continuing this study, this work's attention on a solid solution of strontium molybdate-tungstate [$Sr(Mo_{1-x}W_x)O_4$] crystals with ($x = 0$; 0.25; 0.50; 0.75; and 1), also synthesized by the sonochemical method. However, this time, we have analyzed the effect of substitution in the B-site into the tetragonal lattice, that is, of the Mo^{6+} by the W^{6+} cations, in the structure, morphology, optical, and SPC properties to degrade Rhodamine B (RhB) dye.
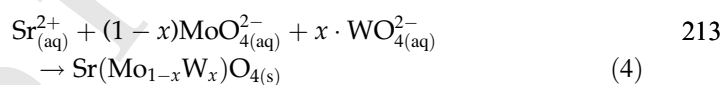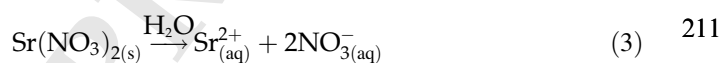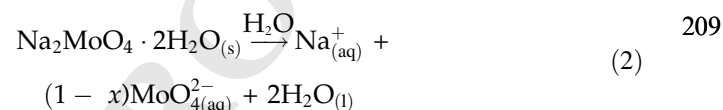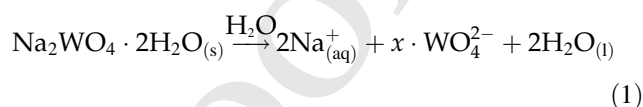
2 Experimental details

2.1 Sonochemical synthesis of solid solution $Sr(Mo_{1-x}W_x)O_4$ crystals

These solid solutions $Sr(Mo_{1-x}W_x)O_4$ crystals with ($x = 0$, 0.25, 0.50, 0.75, and 1) were synthesized by the sonochemical method. In this type of synthetic route, 1×10^{-3} mol of strontium nitrate [$Sr(NO_3)_2$, ACS; 99.0% purity, Synth] was previously dissolved in 50

mL of deionized water and slowly dripped with a graduated burette (approximately one drop/second) in 50 mL of a solution containing $x.1 \times 10^{-3}$ mol of sodium tungstate dihydrate ($Na_2WO_4 \cdot 2H_2O$; 99.0% purity, Sigma–Aldrich) and/or $x.1 \times 10^{-3}$ mol of sodium molybdate dihydrate ($Na_2MoO_4 \cdot 2H_2O$; 99.5% purity, Sigma–Aldrich) according to the desired stoichiometric ratio. This resulting solution was maintained at an average temperature of 40 °C for 3 h using an ultrasonic bath (TABLETOP 402 DIGITAL, Delta Ultrasound).

The following Eqs. (1–4) describe the chemical reactions involved in the formation of the solid solution $Sr(Mo_{1-x}W_x)O_4$ crystals:

$$Na_2WO_4 \cdot 2H_2O_{(s)} \xrightarrow{H_2O} 2Na^+_{(aq)} + x \cdot WO_4^{2-} + 2H_2O_{(l)} \tag{1}$$

$$Na_2MoO_4 \cdot 2H_2O_{(s)} \xrightarrow{H_2O} Na^+_{(aq)} + (1-x)MoO_{4(aq)}^{2-} + 2H_2O_{(l)} \tag{2}$$

$$Sr(NO_3)_{2(s)} \xrightarrow{H_2O} Sr^{2+}_{(aq)} + 2NO^-_{3(aq)} \tag{3}$$

$$Sr^{2+}_{(aq)} + (1-x)MoO_{4(aq)}^{2-} + x \cdot WO_{4(aq)}^{2-} \rightarrow Sr(Mo_{1-x}W_x)O_{4(s)} \tag{4}$$

All suspensions and solid precipitates were washed with deionized water (twenty times) and centrifuged (5000 RPM for 10 min). The precipitates were collected and dried in a muffle furnace (W-One, EDG equipment) at 65 °C for 12 h with a heating rate of 5 °C/min.

2.2 Characterizations

The structural analysis of the solid solution of $Sr(Mo_{1-x}W_x)O_4$ crystals with ($x = 0$, 0.25, 0.50, 0.75, and 1) was performed by means of X-ray diffraction (XRD) and Rietveld refinement. The measurements of X-ray patterns were carried out using a LabX XRD-6000 diffractometer (Shimadzu®, Japan), operating at 40 kV and 20 mA, Cu-Kα radiation (λ = 1.5406 Å) in a 2θ range from 10° to 110° with a scan rate of 1°/min. Rietveld refinement [41] of the measured XRD pattern was carried out using the general structure analysis (GSAS) program [42]. The diffraction peak profiles were adjusted using the Thompson–Cox–Hastings pseudo-Voigt (TCH PV) function and by an asymmetry function, as described by Finger et al.

238 [43]. The background was corrected using a Cheby-
239 shev polynomial of the first order. The strain aniso-
240 tropy broadening was corrected using the
241 phenomenological model described by Stephens [44].
242 The structural data obtained were used to simulate
243 the sample structures through the 3D Visualization
244 for Electronic and Structural Analysis (VESTA) soft-
245 ware, version 3.5.7 for the 64-bit version of Win-
246 dows7® [45, 46]. The analyzes of Raman
247 spectroscopy were carried out in a Senterra II micro-
248 spectrometer (Bruker®, Germany) using a laser with
249 $\lambda = 785$ nm as an excitation source, an output power
250 of 100 mW, the spectral resolution of 3 cm^{-1}, and the
251 range from 50 to 1000 cm^{-1}. Fourier-transform
252 infrared (FT-IR) spectra its obtained in a Vertex 70
253 spectrometer (Bruker®, Germany) ranging from 400
254 to 1000 cm^{-1}, using cesium iodide (CsI) as standard.
255 The particle shapes and sizes are observed in a field-
256 emission scanning electron microscope (FE-SEM),
257 JSM-7100 F (JEOL®, Japan), over an electron accel-
258 eration voltage of 15 kV. Moreover, an elemental
259 analysis or chemical characterization was measured
260 at least five for each sample deposited onto carbon
261 tape through the energy-dispersive X-ray spec-
262 troscopy (EDXS) technique from JEOL®, Japan with a
263 129-eV resolution silicon drift detector with 15 kV
264 accelerating voltage. (see Supplementary Information
265 SI). The optical properties were investigated by UV–
266 Vis spectroscopy on a UV-2600 spectrophotometer
267 (Shimadzu®, Japan) in diffuse reflectance mode.

2.3 Sonophotocatalytic activities measurements

270 The SPC properties of the samples synthesized were
271 investigated for the degradation of RhB dye (C_{28}-
272 $H_{31}ClN_2O_3$, CAS: 81,889, 95% purity, Sigma-Aldrich)
273 in an aqueous solution (1×10^{-5} mol L^{-1}) under UV-
274 C light for 240 min. In these tests, 50 mg of the
275 sample and 100 mL of RhB dye solution were placed
276 in a 250 mL beaker which was then placed inside the
277 ultrasonic bath (M1800 model, BRANSON®, 40 kHz,
278 70 W) and illuminated by four UV-C lamps
279 (OSRAM®, 15 W each, $\lambda_{max} = 254$ nm ≈ 4.88 eV)
280 positioned at a distance of, approximately, 45 cm
281 from the solution. However, before UV-C illumina-
282 tion, the suspensions were only kept under sonica-
283 tion for 5 min in the dark to achieve the adsorption–
284 desorption equilibrium. At intervals of 5, 10, and
285 20 min, aliquots of 2.2 mL were collected and

286 centrifuged (6000 rpm for 20 min) to separate the
287 catalysts from the liquid phase. The variations in the
288 maximum absorption band ($\lambda_{max} = 554$ nm) of RhB
289 solutions were monitored through the UV–Vis
290 absorption spectroscopy on a UV-2600 spectropho-
291 tometer (Shimadzu®, Japan). Equation (5) was used
292 to calculate the catalytic efficiency:

$$\text{Catalytic efficiency of } Sr(Mo_{1-x}W_x)O_4 \text{ crystals (\%)}$$
$$= \frac{C_0 - C_t}{C_0} \times 100,$$

(5)

296 where the C_0 corresponds to the concentrations of
297 RhB dye solution at the beginning and C_t is the
298 concentrations of RhB dye solution at time t. More-
299 over, the photocatalytic (PC) and sonocatalytic (SC)
300 activities of the samples were also investigated, as
301 well as the photolysis (P), sonolysis (S), and
302 sonophotolysis (SP) of RhB dye, to understand the
303 synergistic and individual effects of each system.

2.4 Radical-trapping experiments

305 The participation of reactive species: hydroxyl radical
306 (HO·), superoxide radical ($O_2^{\bullet-}$) and the photogener-
307 ated $e^- \leftrightarrow h^+$ pairs in the SC and SPC of the RhB were
308 investigated by the radical-trapping experiments.
309 Isopropyl alcohol (ISO, C_3H_8O, 99.5% purity, Dinâ-
310 mica), p-benzoquinone (BQ, $C_6H_4O_2$, 98% purity,
311 Dynamics), silver nitrate (AgNO$_3$, 99% purity, Sigma-
312 Aldrich), and ammonium oxalate (AO, $(NH_4)_2$-
313 $C_2O_4 \cdot H_2O$, 99% purity, Dinâmica) were used as scav-
314 engers to trap ·OH, $O_2^{\cdot-}$, e^-, and h^+, respectively.
315 1×10^{-4} mol L^{-1} of scavengers (except the C_3H_8O
316 which was used in the proportion of 1×10^{-1} mol L^{-1})
317 were added to the catalytic reactor only after the 5 min
318 of previous adsorption-desorption assays at dark to
319 start the tests proceeded as described above.

3 Results and discussion

3.1 XRD patterns of solid solution Sr(Mo$_{1-x}$W$_x$)O$_4$ crystals

323 Figure 1a–e shows the XRD patterns of the solid
324 solution Sr(Mo$_{1-x}$W$_x$)O$_4$ crystals ($x = 0$, 0.25, 0.50,
325 0.75, and 1) in the 2θ range from 10 to 70°.

326 For the pure SrMoO$_4$ crystals as displayed in
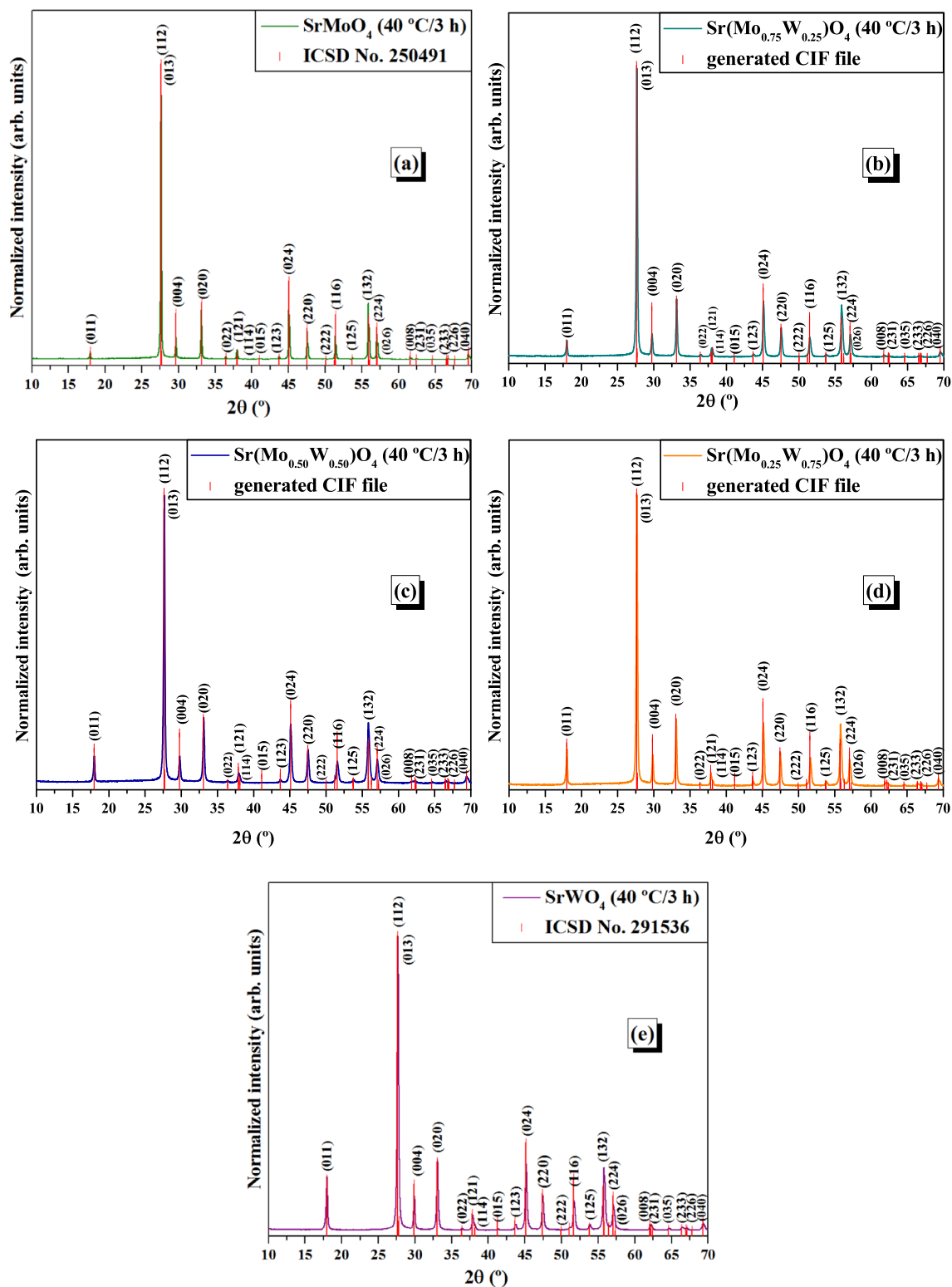327 Fig. 1a, all the diffraction peaks present good

Fig. 1 XRD patterns of **a** SrMoO$_4$, **b** Sr(Mo$_{0.75}$Sr$_{0.25}$)O$_4$, **c** Sr(Mo$_{0.50}$W$_{0.50}$)O$_4$, **d** Sr(Mo$_{0.25}$W$_{0.75}$)O$_4$, and **e** SrWO$_4$ crystals. The vertical lines (∣) denote the respective positions and intensities of XRD peaks described in the ICSD cards No. 250,491, generated CIF files and No. 291,536 for SrMoO$_4$, Sr(Mo$_{1-x}$W$_x$)O$_4$ with ($x = 0.25$; 0.50; 0.75), and SrWO$_4$ phases, respectively

agreement with those registered and reported in the Inorganic Crystal Structure Database (ICSD) card No. 250,491 [47]. Already for our SrWO$_4$ crystals, as shown in Fig. 1e, the diffraction peaks were well-indexed with those registered according to the ICSD card No. 291,536 [48]. These pure crystals presented the scheelite-type tetragonal structure, space group ($I4_1/a$), symmetry point group (C_{4h}^6), four molecular formula units per unit cell (Z = 4), and No. 88 at International Tables of Crystallography. Our solid solutions of Sr(Mo$_{0.25}$W$_{0.75}$)O$_4$, Sr(Mo$_{0.50}$W$_{0.50}$)O$_4$, and Sr(Mo$_{0.75}$W$_{0.25}$)O$_4$ crystals present their crystallographic information files (CIF) generated after Rietveld refinement using both ICSD cards of the samples pure proportionally to the desired stoichiometric information for each one, as shown in Fig. 1b–d and (Supplementary Information SI). It is possible to observe that with the increase in the amount of Mo^{6+} cations, the diffraction peaks located around 18° and 54° almost disappeared, confirming the replacement. These same solid solutions have been reported previously by Li et al. [49] using solvothermal method within the full compositional range (i.e., x from 0 to 1) after being heat-treated at 200 °C for 24 h. These authors have investigated the solid solutions by X-ray diffraction (XRD) and neutron diffraction with good results from Rietveld data. The other peaks exhibit practically identical locations and profiles due to the similarity between the ionic radii of Mo^{6+} and W^{6+} cations (0.41 Å and 0.42 Å, respectively, when the coordination number (CN) for both is 4) [50]. The absence of additional peaks indicates the chemical homogeneity of solid solutions. The sharp diffraction peaks indicate a high crystallinity of oxides materials [51].

3.2 Rietveld refinements of solid solution Sr(Mo$_{1-x}$W$_x$)O$_4$ crystals

Figure 2a–e displays the Rietveld refinement plots of solid solution Sr(Mo$_{1-x}$W$_x$)O$_4$ crystals with (x = 0, 0.25, 0.50, 0.75, and 1) obtained by the sonochemical method.

The structural study and investigation for all solid solutions Sr(Mo$_{1-x}$W$_x$)O$_4$ crystals synthesized by the sonochemical method were performed through XRD with the Rietveld refinement methodology. The measured diffraction patterns were adjusted to the ICSD No. 250,491 [47] and ICSD No. 291,536 [48]. As displayed in Fig. 2a–e, the Rietveld refinement plots of these crystals showing good agreement between the experimentally observed XRD patterns and theoretically fitted results and presented in Table 1, which indicate the success of this method.

The quality index of the structural refinement or Rietveld criteria is also confirmed by low deviations of the statistical parameters (R_{wp}, R_p, R_{Bragg}, and χ^2). The parameters listed in Table 1 indicate that measured diffraction patterns are well adjusted and corroborated by the ICSD No. 250491 [47], and ICSD No. 291536 [48]. Table 1 contains the lattice parameters, unit cell volumes, and site occupancy factor by W and Mo atoms for each solution solid in the crystal lattice calculated by the Rietveld refinement. Moreover, we have compared our results of lattice parameter and unit cell volume presented in Table 1, with this previous paper and observed reasonable agreement [49]. The Rietveld refinement showed that solution solids Sr(Mo$_{1-x}$W$_x$)O$_4$ crystals with (x = 0, 0.25, 0.50, 0.75, and 1) present a scheelite-type tetragonal structure with the Hermann–Mauguin symmetry space group ($I4_1/a$) and four molecular formula units per unit cell (Z = 4), without the presence of secondary phases. Thus, it was proved that there was the substitution of Mo^{6+} for W^{6+} cations in the SrMoO$_4$ crystal lattice, forming solid solutions of Sr(Mo$_{1-x}$W$_x$)O$_4$ crystals. It was also observed that the substitution of Mo^{6+} by W^{6+} ions on the crystal lattice, causes changes in the lattice parameters and consequently in the unit cell volume.

These Rietveld refinement data which contains the Wyckoff positions, site, atomic coordinates (x, y, z) and isotropic thermal parameters (U_{iso}) of Sr, Mo, W, and O atoms for solid solution Sr(Mo$_{1-x}$W$_x$)O$_4$ crystals with (x = 0; 0.25; 0.50; 0.75, and 1) and CIF files, and literature are presented in Table 2.

As can be observed in Table 2, some variations in the atomic positions related to O atoms, while Sr, Mo, and W atoms have fixed atomic positions, which is in good agreement with the literature [47–49]. Our Rietveld refinement data indicate the presence of structural distortions on the tetrahedral [MoO$_4$]/[WO$_4$] clusters, and deltahedral [SrO$_8$] clusters.
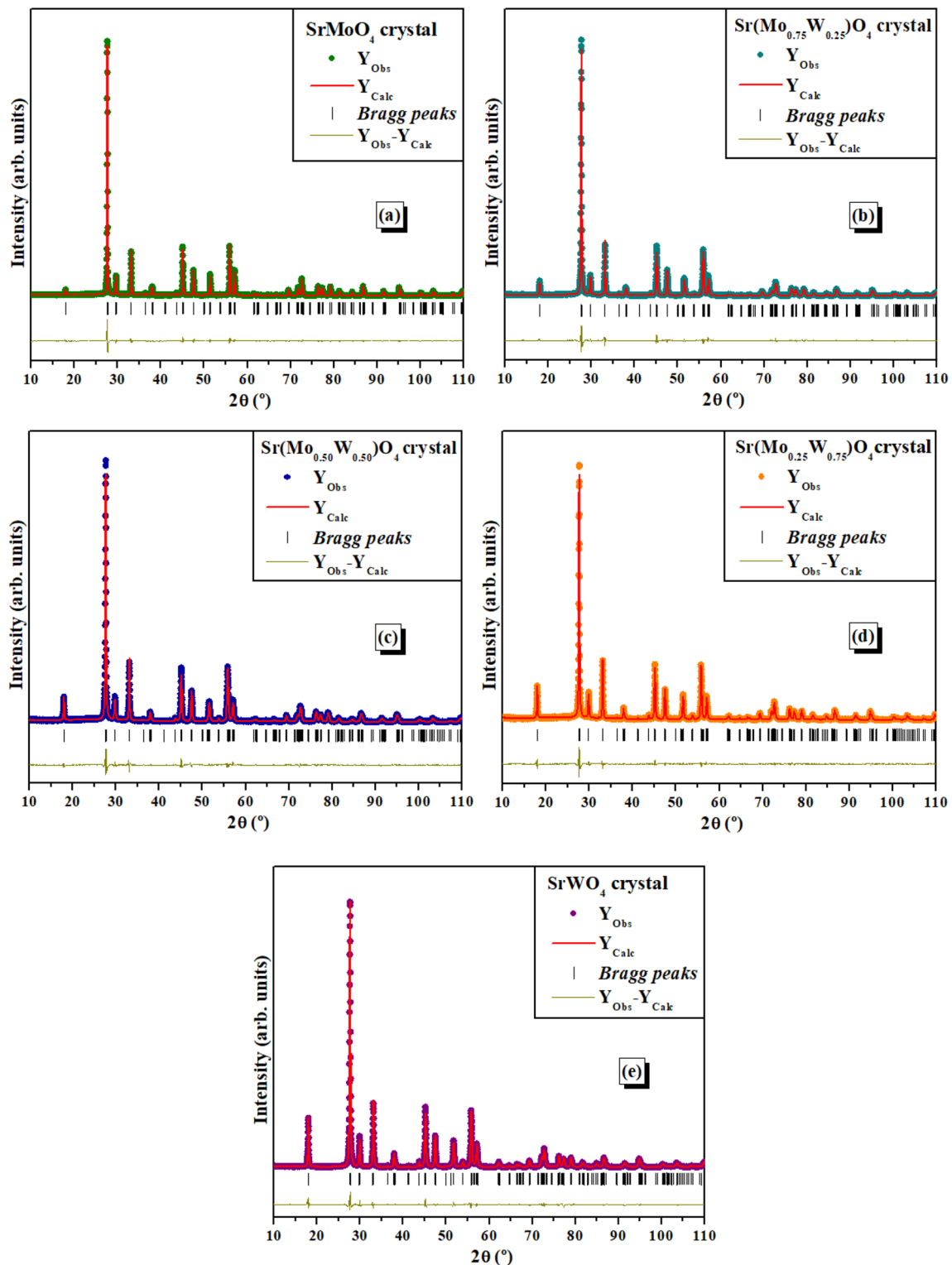
Fig. 2 Rietveld refinement plots of **a** SrMoO$_4$, **b** Sr(Mo$_{0.75}$W$_{0.25}$)O$_4$, **c** Sr(Mo$_{0.50}$W$_{0.50}$)O$_4$, **d** Sr(Mo$_{0.25}$W$_{0.75}$)O$_4$, and **e** SrWO$_4$ crystals, respectively

Table 1 Lattice parameters, unit cell volume, site occupation, and statistical parameters of quality of the solid solution $Sr(Mo_{1-x}W_x)O_4$ crystals with (x = 0; 0.25; 0.50; 0.75; and 1) obtained by Rietveld refinement methodology

Refined formula $Sr(Mo_{1-x}W_x)O_4$	Lattice parameters			Site Occupancy Factors (SOF)		R_{Bragg} (%)	χ^2	R_{wp} (%)	R_p (%)	References [ ]
	a,b (Å)	c (Å)	Unit cell volume (Å^3)	W	Mo					
x = 0	5.404357(27)	12.04033(12)	351.663(4)	0	1	6.294	1.74	9.93	7.56	[⚕]
x = 0.25	5.40818(6)*	12.01880(28)	351.530(8)	0.28	0.72	6.709	1.78	10.13	7.69	[⚕]
x = 0.50	5.41346(6)	11.99928(30)	351.645(9)	0.51	0.49	5.759	1.63	9.32	7.14	[⚕]
x = 0.75	5.41936(5)	11.98283(23)	351.929(7)	0.73	0.27	5.222	1.54	9.26	7.02	[⚕]
x = 1	5.42243(5)	11.96108(21)	351.688(6)	1	0	3.045	1.66	8.86	6.53	[⚕]
ICSD 250,491	5.402647	12.04112(8)	351.45	0	1	–	–	–	–	[47]
ICSD 291,536	5.4268(9)	11.9688(21)	352.48	1	0	–	–	–	–	[48]
x = 0	5.39517	12.01575	–	–	–	–	–	–	–	[49]
x = 0.25	5.39625(36)	11.9939(87)	–	–	–	–	1.04	3.44	3.42	[49]
x = 0.50	5.40284(25)	11.98082(63)	–	–	–	–	1.09	3.72	3.73	[49]
x = 0.75	5.40866(62)	11.96046(149)	–	–	–	–	0.992	5.80	5.67	[49]
x = 1	5.4142	11.9518	–	–	–	–	–	–	–	[49]

[⚕] = This Work, *Ref.* = References reported in the literature; *The numbers in parentheses indicate a shorthand error notation, Example:$a = b$ = 5.40818(6)* or $a = b$ = 5.40818 ($\pm$ 0.000006)

Table 2 Experimental values of the atomic coordinates (x, y, and z) of atoms of solid solutions $Sr(Mo_{1-x}W_x)O_4$ crystals with (x = 0, 0.25, 0.50, 0.75, and 1)

Solution solid of $Sr(Mo_{1-x}W_x)O_4$ crystals	Atoms	Wyckoff	Site	x	y	z	U_{iso}
x = 0	Sr	4b	−4	0	0.25	0.625	0.00900
	Mo	4b	−4	0	0.25	0.125	0.00466
	O	16f	1	0.2319(64)*	0.1183(33)	0.0471(70)	0.01840
x = 0.25	Sr	4b	−4	0	0.25	0.625	0.0114
	Mo	4b	−4	0	0.25	0.125	0.0091
	W	4b	−4	0	0.25	0.125	0.0091
	O	16f	1	0.6333(07)	0.4588(26)	0.2185(12)	0.0414
x = 0.50	Sr	4b	−4	0	0.25	0.625	0.0114
	Mo	4b	−4	0	0.25	0.125	0.0091
	W	4b	−4	0	0.25	0.125	0.0091
	O	16f	1	0.6647(81)	0.4661(50)	0.2085(87)	0.0414
x = 0.75	Sr	4b	−4	0	0.25	0.625	0.0114
	Mo	4b	−4	0	0.25	0.125	0.0091
	W	4b	−4	0	0.25	0.125	0.0091
	O	16f	1	0.6389(68)	0.5102(96)	0.2924(52)	0.0414
x = 1	Sr	4b	−4	0	0.25	0.625	0.0114
	W	4b	−4	0	0.25	0.125	0.0091
	O	16f	1	0.6359(67)	0.4895(18)	0.2934(27)	0.0414

Chemical formula weight for x = 0 (247.56 g/mol); x = 0.25 (272.33 g/mol); x = 0.50 (292.53 g/mol); x = 0.75 (311.88 g/mol); x = 1 (335.47 g/mol). *The numbers in parentheses indicate a shorthand error notation; Example: atomic position for O atom in x = 0.2319(64)* or x = 0.2319(64) ($\pm$0.000064)

3.3 Unit cell representation, lattice parameters, and unit cell volumes values of solid solution $Sr(Mo_{1-x}W_x)O_4$ crystals

Figure 3a–g shows the schematic representations of the unit cells for $SrMoO_4$ crystal, solution solids of $Sr(Mo_{1-x}W_x)O_4$ crystals, $SrWO_4$ crystals, variation in values of the lattice parameters and unit cell volumes as a function of the x value to solution solids crystals, respectively.

As can be observed in Fig. 3a–e, in all unit cells the Mo and W atoms are lattice formers at tetragonal crystal lattice, and are bonded to four O atoms, forming distorted tetrahedral $[MoO_4]$ and/or $[WO_4]$ clusters (4 vertices, 4 faces, and 6 edges) with T_d symmetry point group and different internal (O–Mo–O) and/or (O–W–O) bond angles [52]. However, the solid solutions of $Sr(Mo_{0.75}Sr_{0.25})O_4$, $Sr(Mo_{0.50}W_{0.50})O_4$, and $Sr(Mo_{0.25}W_{0.75})O_4$ crystals exhibit tetrahedral $[MoO_4]/[WO_4]$ clusters more distorted in relation to pure $SrMoO_4$ and $SrWO_4$ crystals. Moreover, in all unit cells the Sr atoms are lattice modifiers and are coordinated to eight O atoms, resulting in distorted deltahedral $[SrO_8]$ clusters (8 vertices, 12 faces, and 18 edges) and D_{2d} symmetry group [53]. As previously discussed, these distortions at the long-range are caused by variations in the (O–Mo–O) and (O–W–O) and (O–Sr–O) bonding angles due to disturbances in the atomic positions at O atoms after the substitution of Mo^{6+} by W^{6+} ions (of greater ionic radius and electronic density), providing different levels of structural order-disorder in crystal lattices [53, 54]. These unit cells exhibit the scheelite-type tetragonal structure, as previously identified by XRD patterns and confirmed by the Rietveld refinement. All structures and clusters were modeled by means of VESTA program (version 3.5.7) using the lattice parameters and atomic positions listed in Tables 1 and 2. Moreover, in Fig. 3f, g an increase can be noted in the lattice parameters ($a = b$ Å), a decrease in the lattice parameter (c Å), and non-linear increase or decrease of unit cell volume (Å^3) values with the substitution of Mo by W. This unusual behavior can be explained due to small diference between the ionic radii of the Mo^{6+} ($r = 0.41$ Å), and W^{6+} ($r = 0.42$ Å) both with same CN = 4. Moreover, our results presented in Tables 1 and 2 can be associated to inter-pretations employing structural refinement which indicate that a small decrease in the lattice parameter

and unit cell volume values is due to the replacement of tetrahedral $[MoO_4]$ by tetrahedral $[WO_4]$ clusters, causing a raise in the electron density in the B-site of the scheelite-type tetragonal structure with general formula ABO_4.

3.4 Micro-Raman and FT-IR spectra of solid solution $Sr(Mo_{1-x}W_x)O_4$ crystals

The Raman spectroscopy technique is of fundamental importance for providing information about the structural order–disorder variations at short range in the crystal lattice of the materials, complementing the data obtained by XRD and Rietveld refinement [55].

According to group theory, molybdate and tungstate crystals with the scheelite-type tetragonal structure present 26 different vibration modes, as described in the following equation:

$$\Gamma = 3A_g + 5A_u + 5B_g + 3B_u + 5E_g + 5E_u \qquad (6)$$

The 13 modes A_g, B_g, and E_g are only active in the Raman spectra, while the modes A_u and E_u are displayed only in the infrared spectra. The three B_u modes are prohibited, and one A_u and one E_u modes are acoustic (of zero frequency). A and B modes are nondegenerate, while E modes are doubly degenerate. The "g" and "u" subscripts indicate the parity under inversion in centrosymmetric crystals [56, 57].

It was noted by means of Raman spectra, the presence of a weak coupling between the ionic groups, which is related to distorted tetrahedral $[MoO_4]$ and/or $[WO_4]$ clusters and the metallic cations, which is related to distorted deltahedral $[SrO_8]$ clusters in the scheelite-type structures.

The vibrational modes active in the characteristic Raman spectra of these crystals can be classified as one of the seven internal modes, which correspond to the oscillations inside the tetrahedral $[MoO_4]$ and/or $[WO_4]$ clusters with an immovable mass center, or as one of the six external modes, which correspond to the motion of the metallic cations in relation to rigid molecular units [58, 59].

Figure 4 shows the Raman spectra of solid solution $Sr(Mo_{1-x}W_x)O_4$ with ($x = 0$; 0.25; 0.50; 0.75; and 1) with the corresponding modes assignments.

Twelve active Raman modes were detected for the $Sr(Mo_{1-x}W_x)O_4$ crystals with ($x = 0$, 0.25, 0.50. 0.75 and 1) samples obtained by the sonochemical method in this work. The intense mode located at 921 cm^{-1}
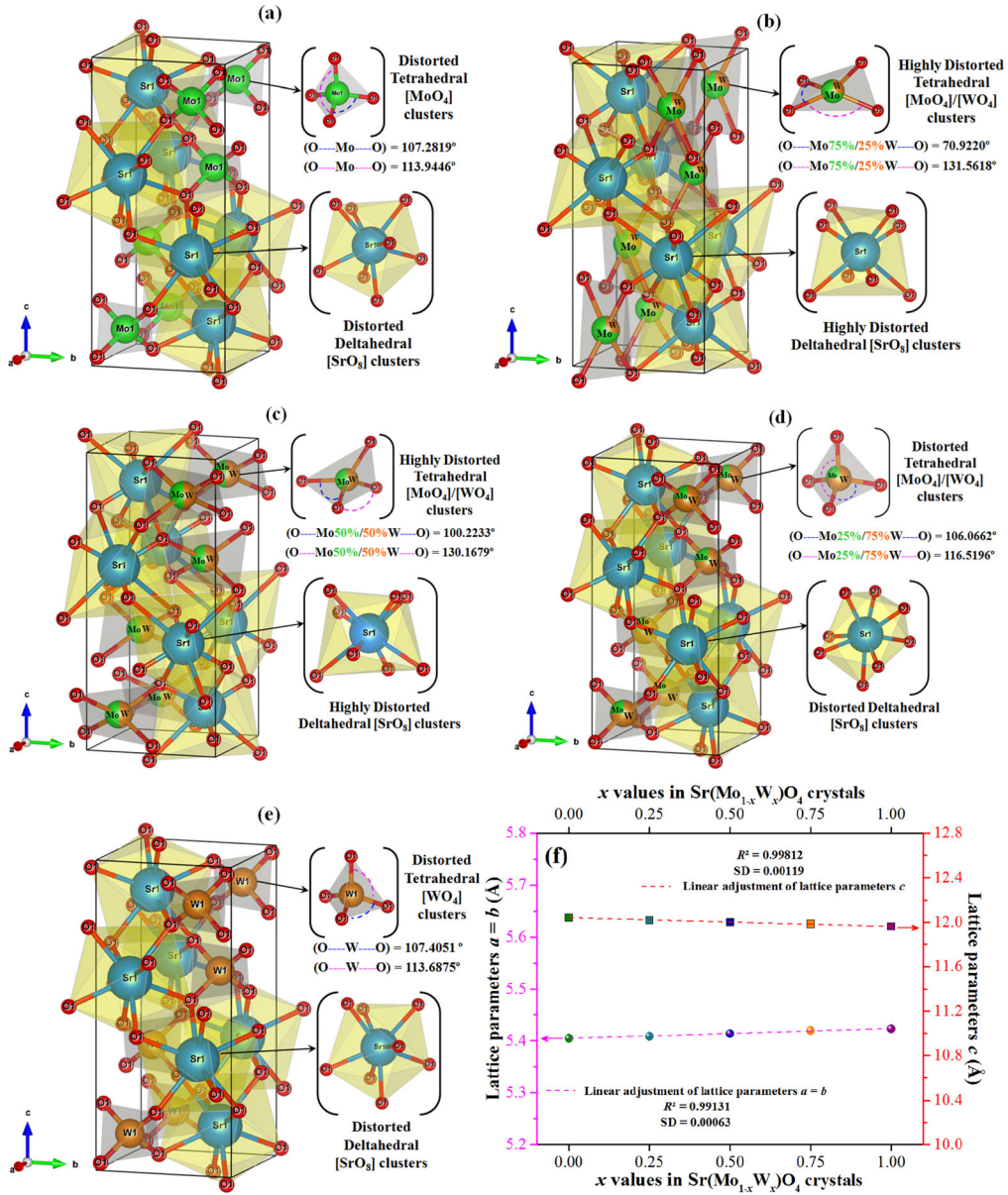
(a) Distorted Tetrahedral [MoO$_4$] clusters
(O——Mo——O) = 107.2819°
(O——Mo——O) = 113.9446°
Distorted Deltahedral [SrO$_8$] clusters

(b) Highly Distorted Tetrahedral [MoO$_4$]/[WO$_4$] clusters
(O——Mo75%/25%W——O) = 70.9220°
(O——Mo75%/25%W——O) = 131.5618°
Highly Distorted Deltahedral [SrO$_8$] clusters

(c) Highly Distorted Tetrahedral [MoO$_4$]/[WO$_4$] clusters
(O——Mo50%/50%W——O) = 100.2233°
(O——Mo50%/50%W——O) = 130.1679°
Highly Distorted Deltahedral [SrO$_8$] clusters

(d) Distorted Tetrahedral [MoO$_4$]/[WO$_4$] clusters
(O——Mo25%/75%W——O) = 106.0662°
(O——Mo25%/75%W——O) = 116.5196°
Distorted Deltahedral [SrO$_8$] clusters

(e) Distorted Tetrahedral [WO$_4$] clusters
(O——W——O) = 107.4051°
(O——W——O) = 113.6875°
Distorted Deltahedral [SrO$_8$] clusters

(f)
R^2 = 0.99812
SD = 0.00119
Linear adjustment of lattice parameters c
Linear adjustment of lattice parameters $a = b$
R^2 = 0.99131
SD = 0.00063
x values in Sr(Mo$_{1-x}$W$_x$)O$_4$ crystals
Lattice parameters $a = b$ (Å)
Lattice parameters c (Å)

(g)
R^2 = 0.23781
SD = 0.11418
Linear adjustment of unit cell volume
Unit cell volumes (Å^3)
x values in Sr(Mo$_{1-x}$W$_x$)O$_4$ crystals

◄**Fig. 3** Schematic representations of the unit cell with scheelite-type tetragonal structures for solid solutions of $Sr(Mo_{1-x}W_x)O_4$ crystals with (**a** $x = 0$, **b** $x = 0.25$, **c** $x = 0.50$, **d** x = 0.75, and **e** $x = 1$), **f** Lattice parameters and **g** unit cell volumes as a function of x concentration at solid solution of $Sr(Mo_{1-x}W_x)O_4$ crystals, respectively

517 (A_g) in the Raman spectrum of $SrWO_4$ and at
518 887 cm^{-1} (A_g) in the Raman spectrum of $SrMoO_4$
519 were attributed to the symmetric stretching vibra-
520 tions of the O–W–O and/or O–Mo–O bonds within
521 the tetrahedral $[WO_4]$ and/or $[MoO_4]$ clusters, as
522 displayed in Fig. 4 and inset of Fig. 4. It is interesting
523 to note that both are present in the Raman spectra of
524 the $Sr(Mo_{0.25}W_{0.75})O_4$, $Sr(Mo_{0.50}W_{0.50})O_4$, and
525 $Sr(Mo_{0.75}W_{0.25})O_4$ samples, whose intensities are
526 directly proportional to the Mo/W ratio. The Raman
527 modes at 837 (B_g) and 798 cm^{-1} (E_g) were attributed
528 to the anti-symmetric stretch vibrations of the O–W–
529 O and/or O–Mo–O bonds. The modes located at 382
530 (E_g) and 372 cm^{-1} (B_g) were associated with anti-
531 symmetric bending vibrations of the O–W–O and/or
532 O–Mo–O bonds, while the mode at 337 cm^{-1} $(A_g +$
533 $B_g)$ was associated with symmetric bending vibra-
534 tions. The modes at 237 cm^{-1} (E_g) and 190 cm^{-1} (B_g)
535 were assigned to the free rotation motions of the
536 distorted tetrahedral $[WO_4]$ and/or $[MoO_4]$ clusters.
537 The external modes generated with the interactions
538 between the Sr^{2+} cations and the distorted tetrahe-
539 dral $[WO_4]$ and/or $[MoO_4]$ clusters are shown
540 between 150 and 65 cm^{-1}, as shown in Fig. 4. The
541 modes around 133 cm^{-1} (E_g) and 75 cm^{-1} (B_g) were
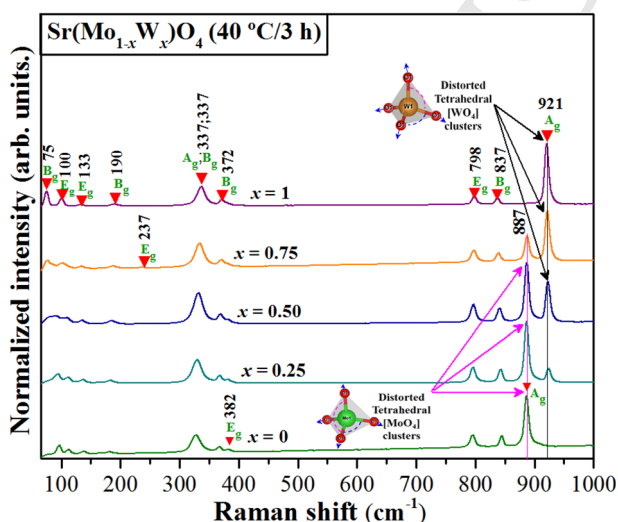
542 assigned to symmetric stretching, and symmetric
543 bending vibrations of O–Sr–O bonds, respectively.
544 The mode around 100 cm^{-1} (E_g) was attributed to
545 free motion (x-, y-, z-axis) of deltahedral $[SrO_8]$ clus-
546 ters [1, 3, 40, 47, 60–62]. Therefore, for all solid solu-
547 tions of $Sr(Mo_{1-x}W_x)O_4$ with ($x = 0$, 0.25, 0.50, 0.75,
548 and 1), the Raman spectra showed characteristic
549 vibrational active modes related to scheelite-type
550 tetragonal structure in good agreement with the lit-
551 erature [54] and our XRD patterns and Rietveld
552 refinement.

553 The FT-IR spectra for the $Sr(Mo_{1-x}W_x)O_4$ crystals
554 with ($x = 0$; 0.25; 0.50; 0.75; and 1), at the wavenum-
555 ber range of 400–1,000 cm^{-1}, are shown in Fig. 5a
556 and inset Fig. 5b in range from 400 to 420 cm^{-1}.

557 Three infrared-active vibrational modes identified
558 were considered internal modes because they origi-
559 nate from movements related to vibrational within
560 the tetrahedral $[MoO_4]$ and/or $[WO_4]$ clusters. The
561 wide and intense band located between 950 and
562 750 cm^{-1} ($1E_u$ and $1A_u$) and a narrow located
563 between 400 and 415 cm^{-1} $[1(A_u + E_u)]$ were attrib-
564 uted, respectively, to the anti-symmetric stretching
565 and symmetric bending vibration of the O–Mo–O
566 and/or O–W–O bonds [12, 40, 63, 64]. The propor-
567 tional replacement of Mo^{6+} by W^{6+} cations promoted
568 a shift in the band close to 400 cm^{-1} for higher
569 wavenumbers. This is due to the difference in elec-
570 tronegativity between the atoms of Mo (2.16) and W
571 (2.36) [65]. Since the W atom is more electronegative,
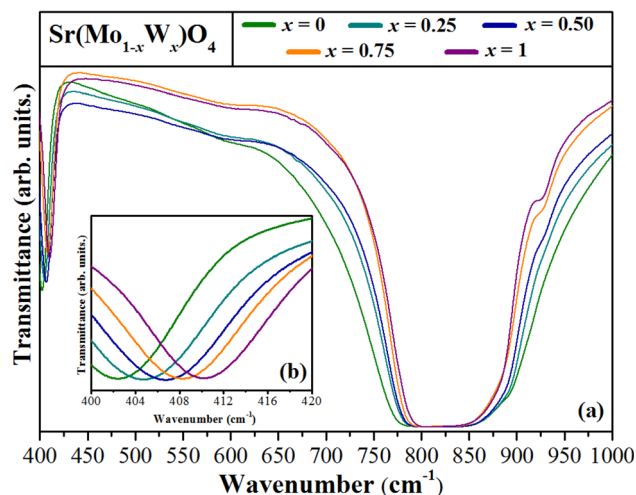572 the O–W–O bond tends to be stronger than the O–

Fig. 4 Raman spectra of solid solution $Sr(Mo_{1-x}W_x)O_4$ crystals with ($x = 0$, 0.25, 0.50, 0.75, and 1)

Fig. 5 a FT-IR spectra of solid solution $Sr(Mo_{1-x}W_x)O_4$ crystals with ($x = 0$, 0.25, 0.50, 0.75, and 1); **b** Inset in FT-IR spectra with magnified in the region from 400 to 420 cm^{-1}

Mo–O bond, so they vibrate at higher frequencies (in regions with higher wavenumbers) [66, 67].

3.5 FE-SEM images analysis of the solid solution of $Sr(Mo_{1-x}W_x)O_4$ crystals

The FE-SEM images of the solid solution $Sr(Mo_{1-x}W_x)O_4$ crystals with ($x = 0$, 0.25, 0.50, 0.75, and 1) are shown in Fig. 6a–j.

As shown in Fig. 6a, b, the $SrMoO_4$ crystals ($x = 0$) formed mostly octahedral-type morphologies (3 µm long and 2 µm wide, approximately) with an apparently smooth surface. Similar results were achieved by Rendón-Angeles et al. [67] through the hydrothermal method and by Jiang et al. [68] also using the sonochemical method. As the x content increased, the octahedron assumed a spindle-like morphology (3 µm long and 1 µm diameter, approximately) with a rougher surface, Fig. 6c–h, until some evolved into dumbbell-like morphologies (3.5 µm long and 1 µm diameter, approximately), predominant in $SrWO_4$ ($x = 1$) crystals, Fig. 6i, j. Mukherjee et al. [69], by the sonochemical method, and Karthik et al. [12], by the co-precipitation method, obtained similar morphologies for $SrWO_4$ crystals. A few star-like and flower-like morphologies also emerged (with a mean size of approximately 3 µm) possibly due to agglomeration of spindle-like morphologies [70]. However, according to Dos Santos et al. [56], star-like morphologies can also arise from a single spindle after dividing its ends, generating new tips and so on, until the morphologies evolve into flower-like crystals. Moreover, we have presented EDX spectra for elemental composition for our five crystals deposited onto carbon tape which are displayed in Fig. SI-1, Fig. SI-2, Fig. SI-3, Fig. SI-4, and Fig. SI-5 (Supplementary Information).

3.6 UV–Vis spectra of the solid solution $Sr(Mo_{1-x}W_x)O_4$ crystals

Figure 7a–e shows the UV–Vis diffuse reflectance spectra of the $Sr(Mo_{1-x}W_x)O_4$ crystals with ($x = 0$, 0.25, 0.50, 0.75, and 1) constructed applying the methodology proposed by Kubelka and Munk [71], as described by De Sousa et al. [40]. In sequence, the E_{gap} values were estimated by extrapolation the linear portion of the spectra to zero absorption coefficient. All spectra showed characteristic profiles of semiconductor crystalline materials with direct transitions between the valence band (VB) and conduction band (CB) [72].

The estimated E_{gap} values of the $Sr(Mo_{1-x}W_x)O_4$ crystals with ($x = 0$, 0.25, 0.50, 0.75, and 1) were 4.27, 4.30, 4.39, 4.53, and 5.01 eV, respectively. The gradual replacement of the Mo^{6+} by the W^{6+} cations caused a directly proportional increase in the E_{gap} values. An expected behavior considering the E_{gap} values reported in the literature for $SrMoO_4$ and $SrWO_4$ crystals. Muralidharan and Sivaji [73] synthesized $SrMoO_4$ and $SrWO_4$ by precipitation method with E_{gap} values of 4.25 and 4.85 eV, respectively. Wang et al. [74] synthesized $SrMoO_4$ by hydrothermal method with E_{gap} of 4.32 eV. Khobragade et al. [75] synthesized $SrWO_4$ by solid-state reaction method with E_{gap} value of 5.80 eV.

It is known that E_{gap} values are associated with the existence of intermediate energy levels within the gap of semiconductor materials that are directly affected by the degree of structural organization of the crystal lattice (oxygen vacancies, binding distortion, and angle deformation) which in turn are affected by synthesis method, particle size, morphology, treatment temperature, and pH of the precursor solution [73]. Therefore, the increase in the E_{gap} value proportional to the replacement of the Mo^{6+} by the W^{6+} cations suggest an increase in the degree of structural organization, although the difference between the ionic radii is small [76].

Dos Santos et al. [56] and Zhang et al. [51] synthesized $SrMoO_4$ microcrystal by the sonochemical method with E_{gap} of 4.05 eV and 3.72 eV, respectively, but, to date, no E_{gap} values associated with $SrWO_4$ crystals synthesized by the sonochemical method on the micro scale have been reported. Theoretical studies estimate E_{gap} values for $SrMoO_4$ crystals between 3.69 and 5.35 eV [5, 77–79] and for $SrWO_4$ between 4.41 and 5.37 eV [80–83]. Therefore, the data discussed so far suggest that the E_{gap} values estimated in this work are within the range of expected values.

### 3.7 Sonophotocatalytic activities of the solid solution $Sr(Mo_{1-x}W_x)O_4$ crystals

The Rhodamine B (RhB) was subjected to different degradation processes and the results obtained are shown in Fig. 8a–d. The degradation rates ($C_t/C_0(\%)$ vs. $t$ime) only under UV-C light (photolysis—P) or
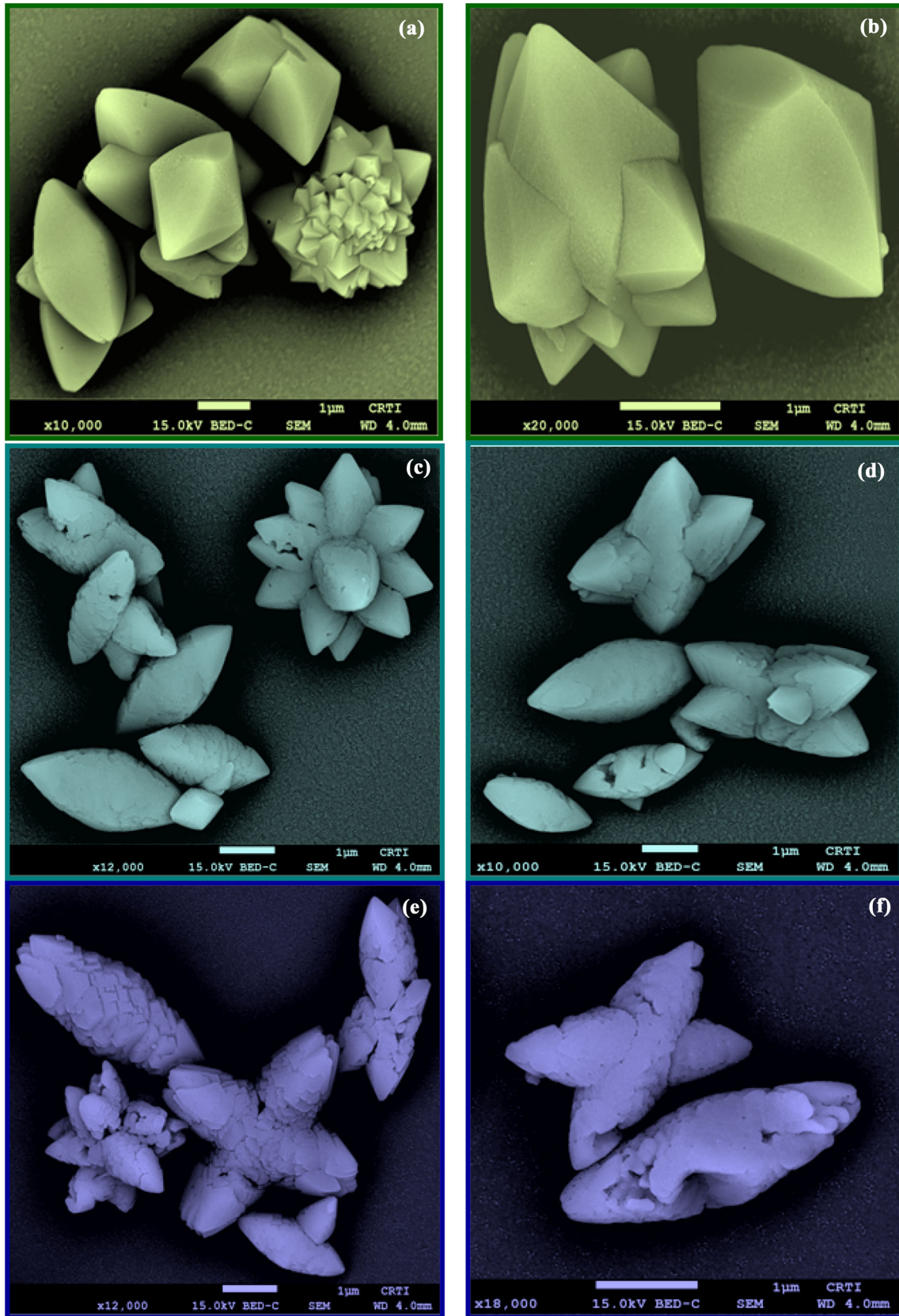
◀ **Fig. 6** FE-SEM images for **a, b** SrMoO$_4$, **c, d** Sr(Mo$_{0.75}$Sr$_{0.25}$)O$_4$, **e, f** Sr(Mo$_{0.50}$W$_{0.50}$)O$_4$, **g, h** Sr(Mo$_{0.25}$W$_{0.75}$)O$_4$, and **i, j** SrWO$_4$ crystals

ultrasonic (sonolysis—S) irradiation, as well as under the combined irradiations (sonophotolysis—SP), is shown in Fig. 8a. Figure 8b, c shows the degradation rates after photocatalysis (PC) and sonophotocatalysis (SPC) process, respectively, using the Sr(Mo$_{1-x}$W$_x$)O$_4$ crystals as catalysts. The percentage of degradation to processes assisted by sonication without and with catalysts is summarized in Fig. 8d.

According to previous papers reported in the literature [2, 5, 10, 13–15, 36], the SrMoO$_4$ and SrWO$_4$ crystals show excellent luminescence and photocatalytic properties. In this way, our focus on the effect of substitution in the *B*-site into the *AB*O$_4$ tetragonal lattice, that is, of the Mo^{6+} by the W^{6+} cations, in the structure, morphology, optical, and improvement of photocatalytic properties against of RhB cationic dye. As can be seen from Fig. 8a, UV-C light alone was not enough to degrade the RhB dye completely (under the conditions employed in this work), since the P process showed a low efficiency of 8%. The addition of the Sr(Mo$_{1-x}$W$_x$)O$_4$ crystals as catalysts to perform the PC process was not effective to degrade a high
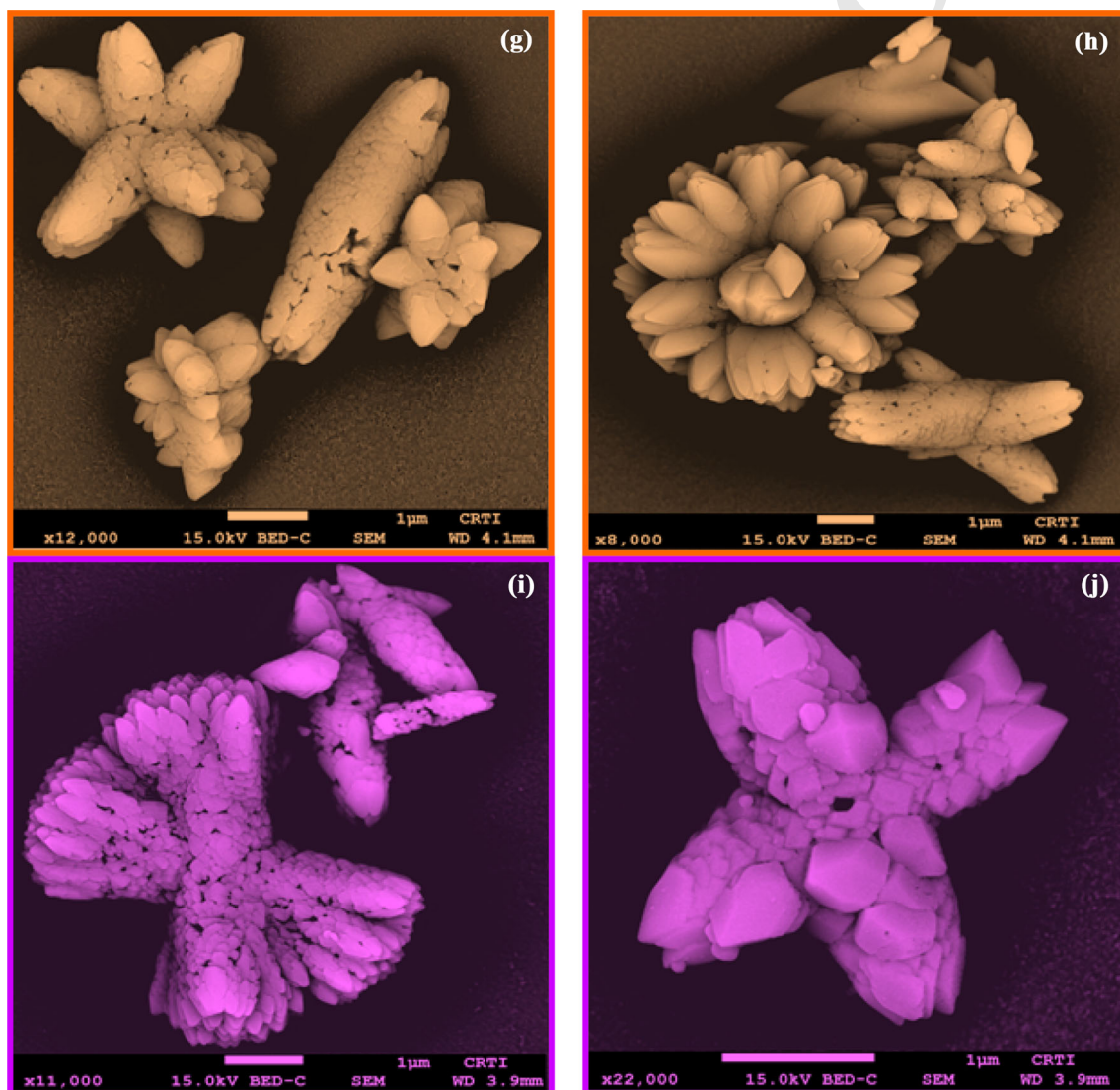
◀ **Fig. 6** continued
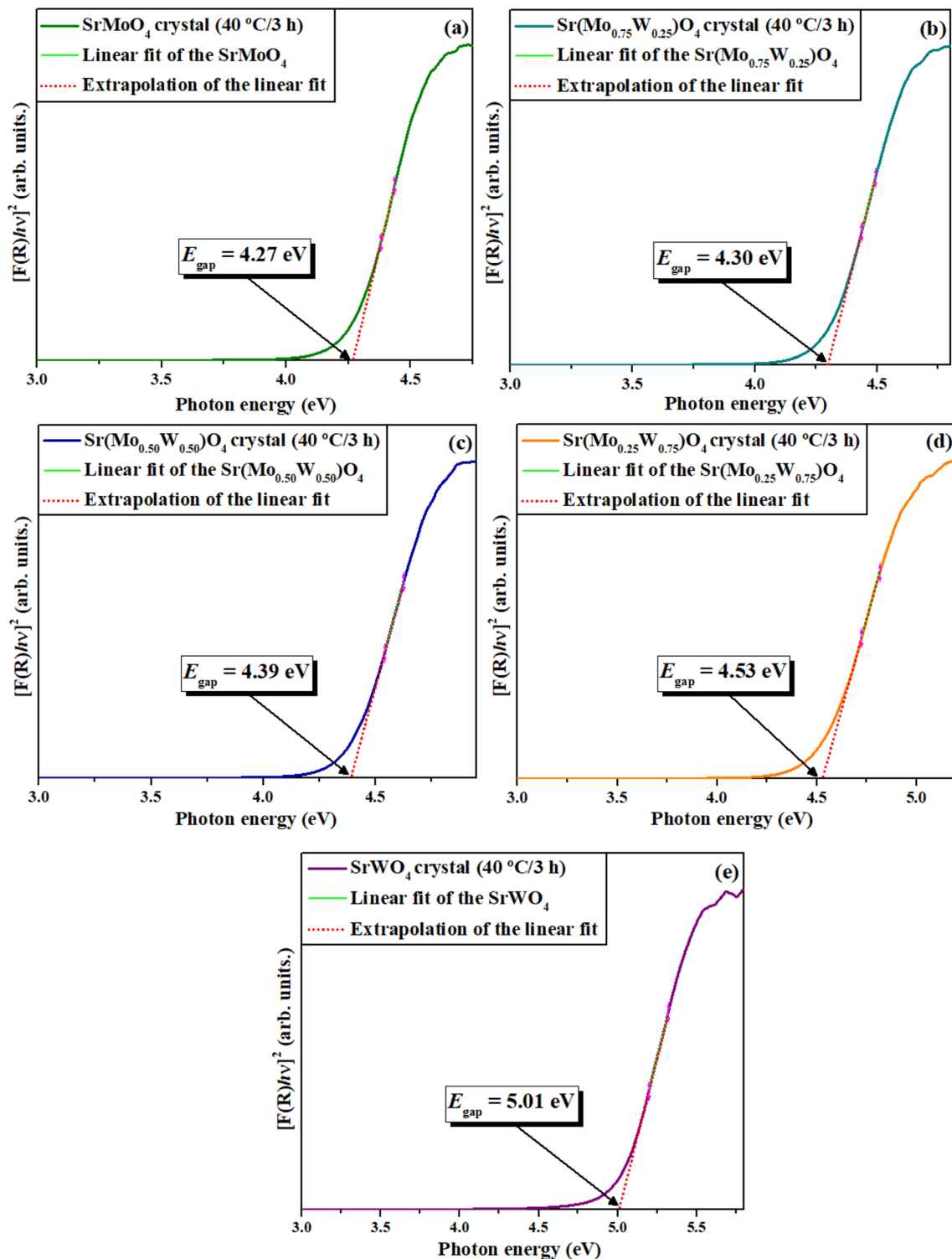
Fig. 7 UV–Vis diffuse reflectance spectra for **a** SrMoO$_4$, **b** Sr(Mo$_{0.75}$Sr$_{0.25}$)O$_4$, **c** Sr(Mo$_{0.50}$W$_{0.50}$)O$_4$, **d** Sr(Mo$_{0.25}$W$_{0.75}$)O$_4$, and **e** SrWO$_4$ crystals, respectively

rate of the RhB cationic dye, indicating a high resistance of this organic molecule, as shown in Fig. 8b. These results are probably due to high recombination rate between the e$^-$↔h$^+$ pairs photogenerated on the surface crystals [84].
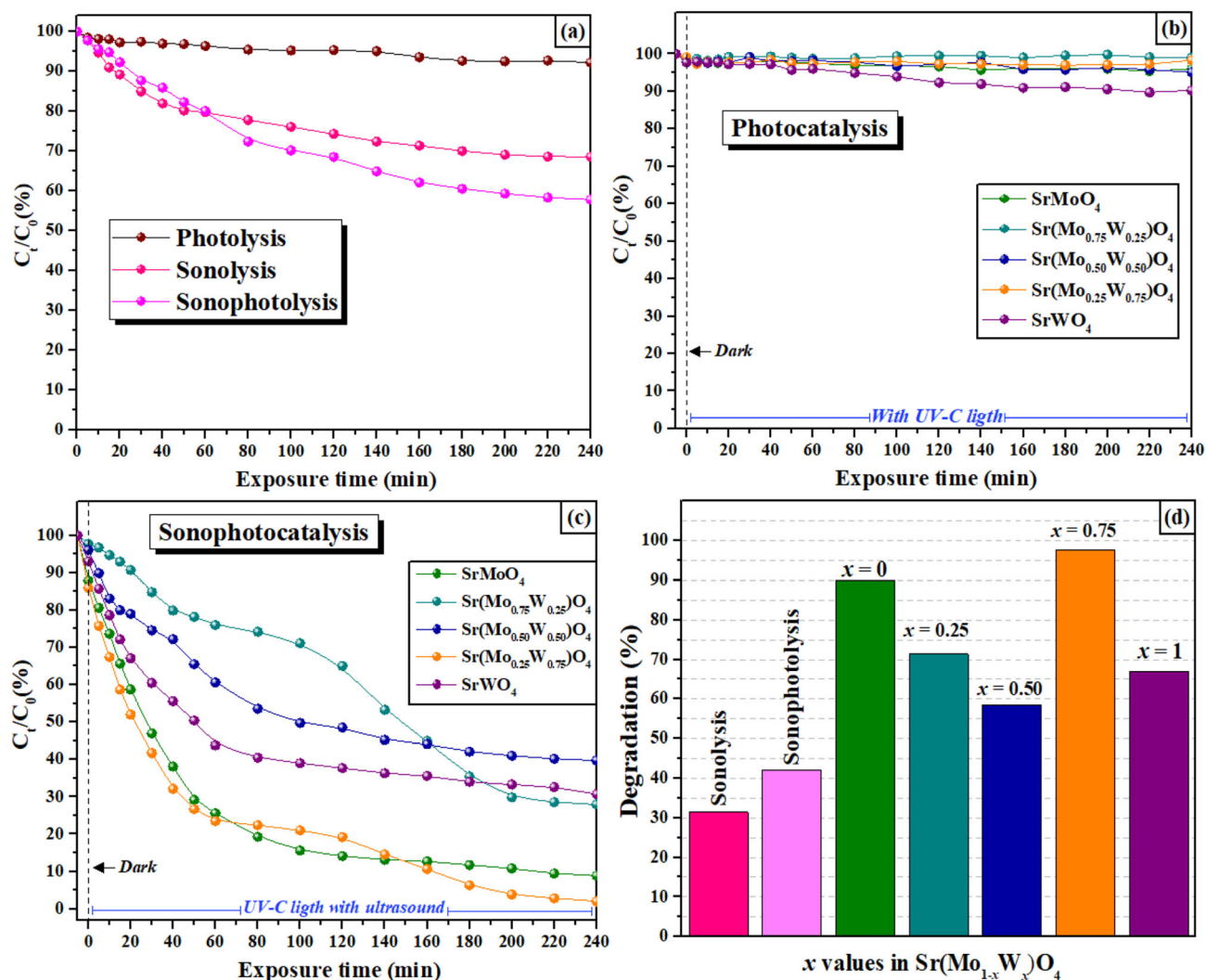
🌀 Springer

Fig. 8 a Photolysis, sonolysis, and sonophotolysis of the RhB dye; **b, c** photocatalysis and sonophotocatalysis using $Sr(Mo_{1-x}W_x)O_4$ crystals with ($x = 0$, 0.25, 0.50, 0.75, and 1) as catalysts; and **d** degradation rate of the sonication-assisted processes, respectively

694 On the other hand, the processes assisted by
695 ultrasonic irradiation proved to be promising, start-
696 ing with S and SP with degradation rates of 31% and
697 42%, respectively. This is due to the appearance of
698 highly reactive species (such as H·, HO· e $HO_2^·$)
699 formed from the cleavage of H_2O and dissolved O_2
700 molecules during acoustic cavitation events. How-
701 ever, it is known that the thermolytic degradation of
702 the pollutant is also an option, given the high tem-
703 peratures generated after the collapse of the cavita-
704 tion bubbles [85].
705 The SP confirmed the benefits of the simultaneous
706 use of UV-C light and ultrasonic irradiation and,
707 after addition of $Sr(Mo_{1-x}W_x)O_4$ crystals as catalysts,
708 a synergistic effect was observed during SPC process
709 of the RhB dye as illustrated in Fig. 8c. This effect is

710 due to the ability of the combined systems (ultra-
711 sound, light, and catalyst) to compensate for the
712 deficiencies presented by each degradation process
713 [86].
714 One of the limitations of the photocatalysis is the
715 high recombination rate between $e^- \leftrightarrow h^+$ pairs pho-
716 togenerated on the catalyst surface, but reactive
717 species formed during sonolysis can delay this
718 recombination, contributing to the generation of more
719 reactive species. Furthermore, the shock waves cre-
720 ated after implosion of cavitation bubbles (i) lead to
721 fragmentation and deagglomeration of catalyst par-
722 ticles, increasing their surface area; (ii) contribute to
723 the continued cleaning of their active catalytic sites,
724 preventing the accumulation of organic pollutants
725 and their intermediates produced during

726 degradation; and (iii) accelerate the mass transfer
727 between the organic pollutants and the catalyst sur-
728 face. Meanwhile, the catalysts can act as additional
729 cores to form more cavitation bubbles potentiating all
730 the effects previously mentioned [31, 87].

731 The better SPC performance was observed for the
732 Sr(Mo$_{0.25}$W$_{0.75}$)O$_4$ crystals (98%) followed by SrMoO$_4$
733 (90%), SrMo$_{(0.75}$W$_{0.25)}$O$_4$ (71%), SrWO$_4$ (67%), and
734 Sr(Mo$_{0.50}$W$_{0.50}$)O$_4$ crystals (59%). From Fig. 8d, it can
735 be inferred that starting from pure SrMoO$_4$ crystals,
736 such a sequence seems to be inversely proportional to
737 the increase of the x value and raise of E_{gap} value,
738 with the exception of the Sr(Mo$_{0.25}$W$_{0.75}$)O$_4$ crystal. In
739 view of this and based on our structural data, clusters
740 modeling, FE-SEM images, and UV–Vis spectrum,
741 we can attribute that the solid solution Sr(Mo$_{0.25}$-
742 W$_{0.75}$)O$_4$ crystals exhibit favorable conditions to the
743 best performance catalytic, as specific defects on the
744 crystal surfaces, optical band gap values near the
745 energy (4.88 eV) of UV-C illumination, several pores
746 and high surface roughness can present high surface
747 area inducing the appearance of more active catalytic
748 sites. So, its structural organization seems to be ide-
749 ally favorable (among the conditions investigated in
750 this work) to achieve the highest SPC performance.
751 Therefore, it was the catalyst chosen to carry out the
752 concentration tests, the results of which are shown in
753 Fig. 9, in order to find the best proportion between
754 the amount of catalyst (25, 50, 75, and 100 mg) and
755 volume of solution (100 mL) in the SPC of RhB dye.

756 The SPC degradation rate increased proportionally
757 to the increase in the amount of catalyst up to the
758 ratio of 50 mg/100 mL, and thereafter it decreased in
759 the same proportion, as shown in Fig. 9. This may be
760 related to the fact that when the catalyst dosage
761 increases, the number of available active sites as well
762 as additional nuclei for the formation of cavitation
763 bubbles also increases, increasing the production of
764 oxidizing radicals and, therefore, the rate of degra-
765 dation. However, this synchronism seems to be effi-
766 cient to a certain extent: as the catalyst dosage
767 increases, even more, the particle deagglomeration
768 process seems to lose its efficiency, decreasing the
769 catalyst surface area and, consequently, the number
770 of active sites. Furthermore, catalyst concentration
771 beyond an ideal value can cause light scattering due
772 to increased solution turbidity, making it difficult for
773 some catalyst particles to absorb light, thus reducing
774 degradation efficiency [86, 88, 89].
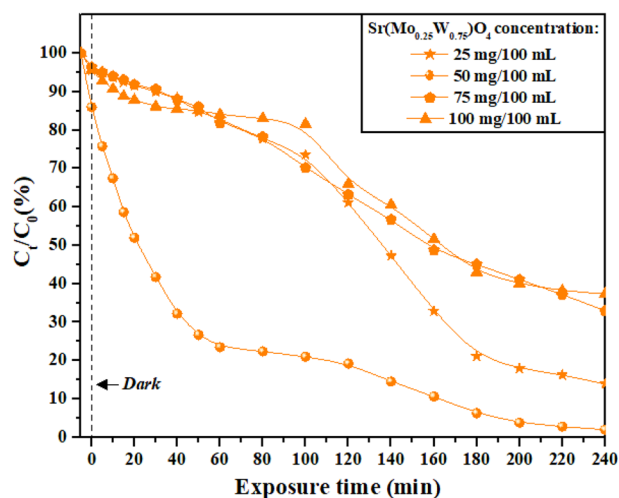
Fig. 9 Catalytic assays with concentration effect between the catalyst of the solid solutions Sr(Mo$_{0.25}$W$_{0.75}$)O$_4$ crystals with 25, 50, 75, and 100 mg, and the RhB dye solution (100 mL)

775 After discovering the ideal ratio (under the condi-
776 tions of this work) and confirming the synergistic
777 effect during SPC process, Sr(Mo$_{0.25}$W$_{0.75}$)O$_4$ crystals
778 were also used in the sonocatalysis (SC- only ultra-
779 sound and catalyst) of the RhB dye, and the data are
780 displayed in Fig. 10.

781 The SC process presented a considerable degrada-
782 tion rate of 76% (2.45 times greater than S process).
783 However, as expected, the degradation efficiency in
784 the SPC process was superior to all other processes.
785 In general, photogenerated e$^-$↔h$^+$ pairs and super-
786 oxide (O$_2^{\cdot-}$) and hydroxyl (HO$^\cdot$) radicals are the
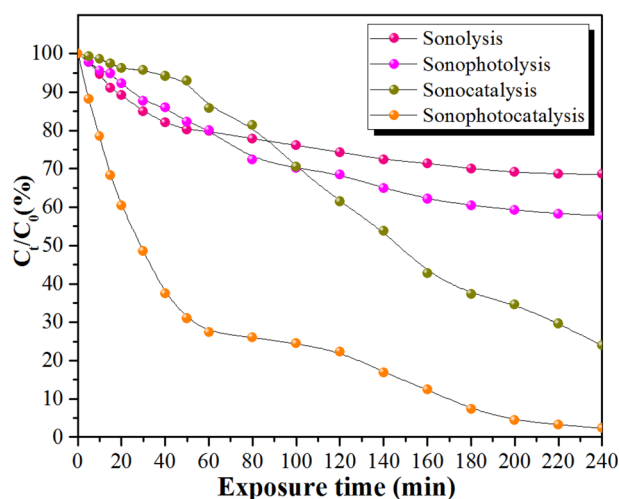
Fig. 10 Sonolysis, sonophotolysis, sonocatalysis, and sonophotocatalysis of the RhB dye using the Sr(Mo$_{0.25}$W$_{0.75}$)O$_4$ crystals as catalysts in the proportion of 50 mg/100 mL

⚇ Springer

predominant reactive species in the degradation process, as shown in Fig. 10.

However, to determine the main species during SC and SPC processes with $Sr(Mo_{0.25}W_{0.75})O_4$ crystals (in the proportion of 50 mg/100 mL), experiments were carried out with AO, $AgNO_3$, BQ, and ISO scavengers of h^+, e^-, $O_2^{\cdot-}$, and $HO^{\cdot}$ radicals, respectively. These results are shown in Fig. 11.

The inhibition of RhB dye degradation in both SC and SPC process was not as pronounced after addition of AO and $AgNO_3$ showing that the photogenerated $e^- \leftrightarrow h^+$ pairs are not the main reactive species in both processes, although they contribute to a certain degree, even in the absence of UV-C light, which can be explained by the phenomenon of sonoluminescence. When the light energy emitted during sonoluminescence equals or exceeds the E_{gap} of the catalyst, e^- can be excited from VB to CB and generate $e^- \leftrightarrow h^+$ pairs [32, 90, 91].

In SC process, the lowest rate of inhibition was observed after addition of BQ, indicating that the $O_2^{\cdot-}$ radical is the least participative reactive species, possibly because it is present in a smaller amount, as shown in Fig. 11. The opposite was observed during SPC, which was shown to be the main species, followed by the $HO^{\cdot}$ radicals. Most of the $O_2^{\cdot-}$ radicals are formed by e^- in CB, generated in greater numbers in SPC process due to the presence of UV-C light [92]. As expected, in SC the $HO^{\bullet}$ radical was shown to be the main degradation agent.

Figure 12a–d shows the UV–Vis spectra of the RhB dye after the S, SP SC, and SPC processes using the solid solution of $Sr(Mo_{0.25}W_{0.75})O_4$ crystals as a catalyst.

Displacements in the RhB dye maximum absorption bands at $\lambda_{max} = 554$ nm (characteristic of the chromophore group) were not observed in any of the processes, suggesting that there was no formation of secondary products [93]. Its considerable reduction, as well as the more discrete band located at 259 nm (attributed to aromatic rings), during SPC process is one of the indications of complete mineralization of RhB dye [94]. Therefore, the solution solid $Sr(Mo_{0.25}W_{0.75})O_4$ crystals displayed the best sonophotocatalytic activity to degradation rate of 98% in 240 min to RhB dye, as shown in Fig. 12. Finally, we compare our new results obtained in this work for the solid solutions $Sr(Mo_{1-x}W_x)O_4$ crystals with ($x = 0$, 0.25, 0.50, 0.75, and 1) in relation to previous works reported in the literature [95–107], which has been presented in Table 3.

As presented in Table 3, we have noted some well significant differences in degradation rate by the photocatalytic and sonophotocatalytic activity of pure $SrMoO_4$ and $SrWO_4$ crystals and solid solutions of $Sr(Mo_{0.25}W_{0.75})O_4$, $Sr(Mo_{0.50}W_{0.50})O_4$, and $Sr(Mo_{0.75}W_{0.25})O_4$ crystals compared to other works reported in the literature [95–107]. These differences in degradation rate among other semiconductor crystals with correlated structures reported before in the literature are ascribed to different factors, such as intermediary electronic levels, order-disorder at the crystalline lattice, oxygen vacancies, roughness, high surface energy, defects, high active surface area, facets, and adsorption-desorption equilibrium. Moreover, the main factor responsible for the high-efficiency photocatalysis of the catalyst crystals is the low recombination rate between photogenerated $e^- \leftrightarrow h^+$ pairs on the semiconductor surface.

4 Conclusion

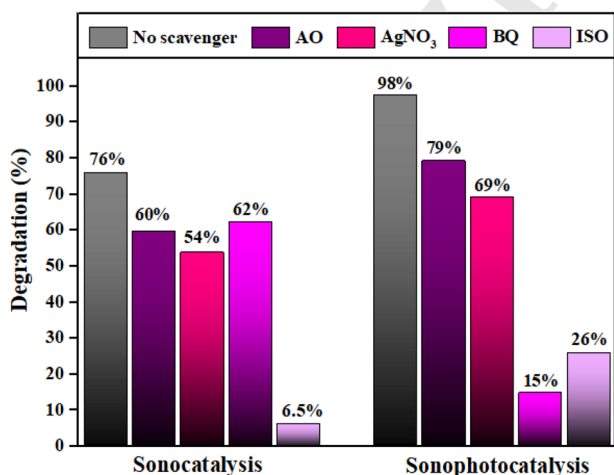In summary, the solution solid of $Sr(Mo_{1-x}W_x)O_4$ crystals with ($x = 0$, 0.25; 0.50, 0.75, and 1) were synthesized with success by means of sonochemical method at 40 °C for 3 h. These experimental investigations indicate that our sonochemical method, pre-homogenizing, and sonicating the systems constantly (drop by drop) allows the formation of a pure solid solution $Sr(Mo_{1-x}W_x)O_4$ crystals more effectively than the conventional precipitation method at room
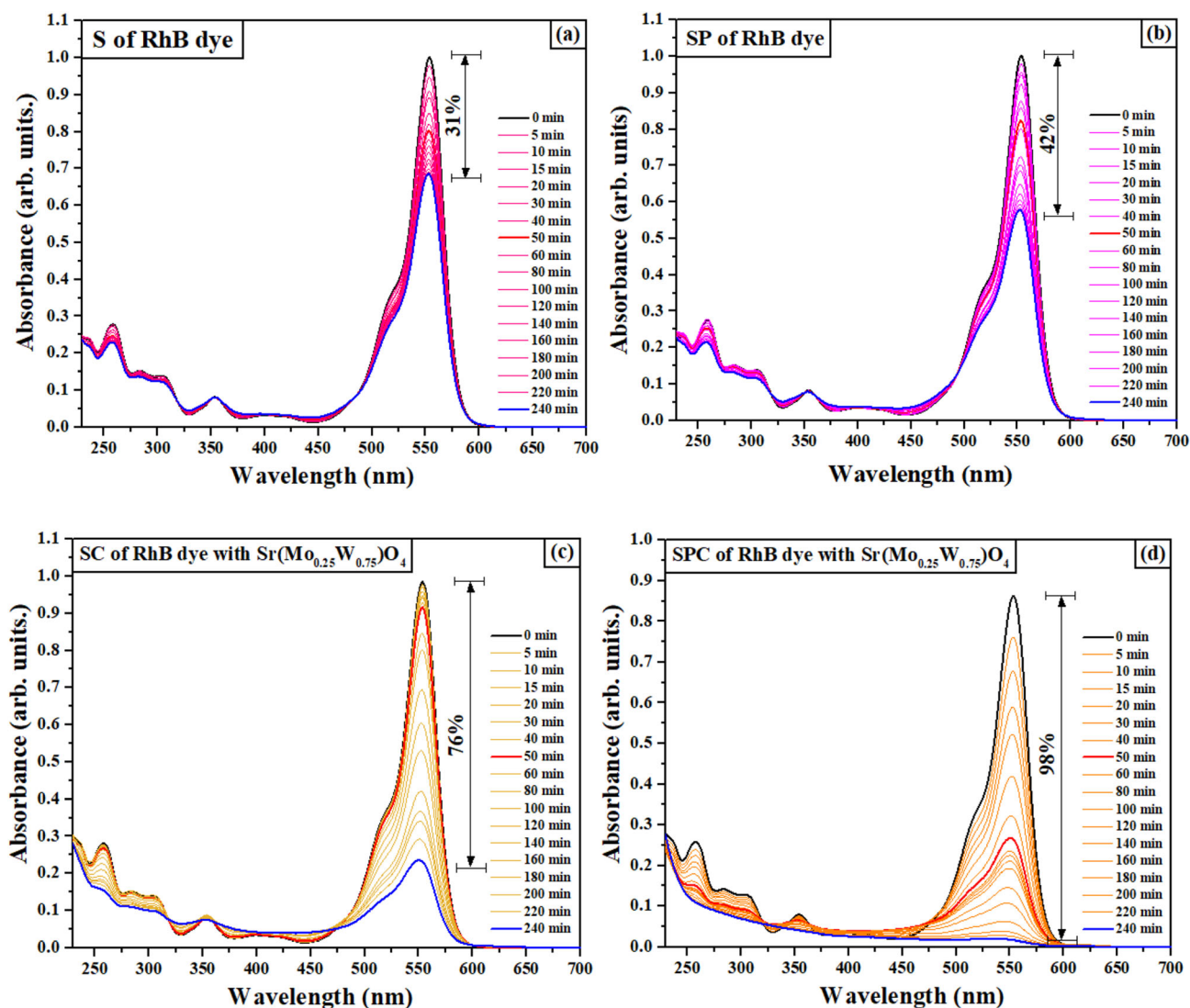

Fig. 11 Effects of different scavengers on the SC and SPC process to degrade RhB dye

Fig. 12 UV–Vis absorption spectra of RhB dye solution after **a** S, **b** SP, **c** SC, and **d** SPC processes using $Sr(Mo_{0.25}W_{0.75})O_4$ crystals as catalysts, respectively

temperature. All our crystals present a scheelite-type tetragonal structure with pure phases and crystalline as confirmed by the XRD patterns and proved by Rietveld refinement data. The Raman and FT-IR spectra exhibit symmetrical and asymmetrical stretching and bending modes and bands characteristics, corroborating the XRD patterns and Rietveld refinement data. The $SrMoO_4$ crystals showed octahedral-like morphologies that assumed a spindle-like shape as the replacement of the Mo^{6+} by the W^{6+} cations happened until they assumed a dumbbell-like morphology for the pure $SrWO_4$ crystals. FE-SEM images display some star- and flower-like morphologies which are possibly due to agglomeration of spindle-like morphologies. Therefore, based on these

observations of the FE-SEM images for the morphology, it has been verified that the $SrMoO_4$ crystals present a more defined shape as octahedra and more homogeneous facets, possibly indicating crystallographic facets with high surface energy for catalysis. However, it is also well known in the literature that oxide materials with the presence of several pores and high surface roughness can present high surface area inducing the appearance of more active catalytic sites, which is the case of $Sr(Mo_{0.25}W_{0.75})O_4$ crystals. Finally, good sonophotocatalytic performances were obtained for $SrMoO_4$ crystals (90%), and mainly to $Sr(Mo_{0.25}W_{0.75})O_4$ crystals (98%). EDXS data were used for analyses of chemical composition of the solid solution. The E_{gap} values of the materials varied

⚛ Springer

Table 3 Degradation rate by the photocatalytic and sonophotocatalytic activity of solid solutions $Sr(Mo_{1-x}W_x)O_4$ crystals with ($x = 0$, 0.25, 0.50, 0.75, and 1) reported in the literature and compared with the present work Ξ

Crystal	Synthesis method	Pollutant type	Concentration (mol L^{-1})	Degradation rate (%)	End Time (min)	References
SrMoO$_4$	Simple solvothermal	Salicilic Acid	2.5×10^{-4}	~ 5	150	[95]
		Rhodamine B	1×10^{-5}	~ 15	120	
SrMoO$_4$	Sonochemical	Methyl Orange	3.06×10^{-5}	71	60	[96]
SrMoO$_4$	Precipitation	Diphenylamine	1.18×10^{-1}	99	45	[97]
SrMoO$_4$	Precipitation	Methyl Orange	1.53×10^{-4}	83	80	[98]
SrMoO$_4$	Hydrothermal	Methylene Blue	3.13×10^{-5}	50	120	[99]
SrMoO$_4$	Conventional termal decomposition	Methylene Blue	3.13×10^{-5}	98	120	[100]
SrMoO$_4$	Solid-state	Tetracycline	2.25×10^{-5}	79 88	180	[101]
SrMoO$_4$	Termal decomposition	Methylene Blue	3.13×10^{-5}	93	120	[102]
SrMoO$_4$	Standard ceramic processing technique	Rhodamine B	5.2×10^{-2}	20	30	[103]
SrMoO$_4$	Hydrothermal	Methylene Blue	3.13×10^{-5}	93.29	140	[104]
SrMoO$_4$	Hydrothermal	Methylene Blue	3.13×10^{-5}	64.8	120	[105]
SrMoO$_4$	Hydrothermal	Cr(VI)	10 ppm	< 5	180	[106]
SrMoO$_4$	Hydrothermal	Methylene Blue	3.13×10^{-5}	64.8	120	[107]
SrMoO$_4$	Sonochemical	Rhodamine B	1×10^{-5}	90	240	[Ξ]
$Sr(Mo_{0.75}W_{0.25})O_4$	Sonochemical	Rhodamine B	1×10^{-5}	71	240	[Ξ]
$Sr(Mo_{0.50}W_{0.50})O_4$	Sonochemical	Rhodamine B	1×10^{-5}	59	240	[Ξ]
$Sr(Mo_{0.25}W_{0.75})O_4$	Sonochemical	Rhodamine B	1×10^{-5}	98 75	240	[Ξ]
SrWO$_4$	Sonochemical	Rhodamine B	1×10^{-5}	67	240	[Ξ]

directly proportional to the substitution of the Mo^{6+} by the W^{6+} cations from 4.27 to 5.01 eV, suggesting an increase in the structural organization with the substitution. The high efficiency for degradation of the RhB dye was achieved during the SPC process using the $Sr(Mo_{0.25}W_{0.75})O_4$ crystals as a catalyst in the proportion of 50 mg/100 mL. The O$_2{}^{.-}$ radicals were shown to be the main degradation agent in the SPC process, while for the SC process, it was the HO$^{.}$ radicals.

Author contributions

This manuscript was written through the contributions of all authors that agreed with this submission.

PBdeS, FHPL, and BSS prepared the samples and performed the UV–Vis measurements and photocatalytic assays. ICN performed the Rietveld refinement and structural analysis. GOMG and SBSG performed the Raman, and FT-IR measurements. JCS, AFG, and LSC conceived the project. All authors participated in writing the manuscript and discussing all the results.

Funding

The authors do have not any funding to pay for open access.

Data availability

The data that support the findings of this study are available on request from the corresponding author.

Declarations

Conflict of interest The authors declare that they have no conflict of interest.

Supplementary Information: The online version contains supplementary material available at http s://doi.org/10.1007/s10854-022-08985-1.

References

1. A. Azzouzi, M. Benchikhi, R. El Ouatib, Room-temperature co-precipitation synthesis of (Ca,Sr,Ba)WO_4 solid solutions: Structural refinement, morphology and band gap tuning. Ceram. Int. **46**, 23706–23718 (2020)

2. S.K. Swain, G. Phaomei, S.K. Tripathy, N. Yaiphaba, R.B. Devi, S. Nayak, B.B. Parida, Effect of β-cyclodextrin decoration on structural, optical and magnetic properties of luminescent magnetic nanoparticles and its application as a drug carrier. J. Mol. Struct. **1247**, 131330-1–131330-6 (2022)

3. S. Swathi, R. Yuvakkumar, P.S. Kumar, G. Ravi, D. Nanthini, D. Velauthapillai, Flower like strontium molybdate for efficient energy conversion applications. Fuel **308**, 122051-1–122051-8 (2008)

4. R. Ashraf, Z. Shehzadi, T. Mahmood, S. Naeem, N. Shehzadi, S. iftikhar, Z. Parveen (2021) DFT based investigations of BaWO_4: electronic and optical properties. Phys. B Phys. Condens. Matter 621: 413309-1-413309-5

5. M. Benzineb, F. Chiker, H. Khachai, H. Meradji, S. Uğur, S.H. Naqib, S.B. Omran, X. Wang, R. Khenata, A comparative study of structural, thermal, and optoelectronic properties between zircon and scheelite type structures in SrMoO_4 compound: an ab-initio study. Optik **238**, 166714-1-166714-13 (2021)

6. N. Karuppusamy, V. Mariyappan, T.W. Chen, S.M. Chen, R. Sundaresan, S.P. Rwei, X. Liu, J. Yu, Scheelite type barium tungstate nanoparticles decorated on graphitic carbon nitride nanocomposite for the detection of diphenylamine in apple juice. Int. J. Electrochem. Sci. **16**, 210830-1–2108302-0 (2021)

7. Z.A. Mikhaylovskaya, E.S. Buyanova, E.V. Sokolenko, G.V. Sliusarev, S.A. Petrova, A.F. Zatsepin, Effect of bismuth addition on the crystal and electronic structure of strontium molybdate. Russ. J. Phys. Chem. A **94**, 2502–2509 (2020)

8. A. Verma, S.K. Sharma, Rare-earth doped/codoped CaMoO_4 phosphors: a candidate for solar spectrum conversion. Solid State Sci. **96**, 105945-1–105945-10 (2019)

9. P. Yadav, P. Dev Bhuyan, S.K. Rout, Y. Sonvane, S.K. Gupta, E. Sinha, Mater. Today Commun. **25**, 101417-1–101417-12 (2020)

10. S. Saravanakumar, D. Sivaganesh, V. Sivakumar, S. Sasikumar, T.K. Thirumalaisamy, M.A. Sayed, A.M. Ali, Red emitting Eu^{3+} induced SrWO_4 materials: synthesis, structural, morphological and photoluminescence analysis. Phys. Scr. **96**, 125817-1–125817-15 (2021)

11. R. Gopal, J. Manam, Mater. Today Proc. **46**, 6185–6190 (2021)

12. R. Karthik, P.M. Shafi, S.M. Chen, R. Sukanya, G. Dhakal, J.J. Shim, Investigation on microstructural impacts to electrochemical performances of strontium tungstate as efficient bifunctional catalyst for hydrogen and oxygen evolution reactions. J. Taiwan. Inst. Chem. Eng. **126**, 145–153 (2021)

13. A.B. Chavan, A.B. Gawande, V.B. Gaikwad, G.H. Jain, M.K. Deore, Hydrothermal synthesis and luminescence properties of Dy^{3+}doped SrMoO_4 nano-phosphor. J. Lumin. **234**, 117996-1-17996-8 (2021)

14. B.G. Vats, M. Shafeeq, S. Kesari (2021) Triple molybdates and tungstates scheelite structures: effect of cations on structure, band-gap and photoluminescence properties. J. Alloys Compd. 865: 158818-1-158818-9

15. H. Gao, Y. Wang, Q. Gao, X. Pan, S. Wang, H. Yang, C. Chen, Y. Wang, L. Fang, Z. Yi, Phase evolution and photoluminescence behavior of MMoO_4 (M = Mg, Ca, Sr) phosphors. Optik **241**, 167040-1-167040-13 (2021)

16. S. Zinatloo-Ajabshir, M. Baladi, O. Amiri, M. Salavati-Niasari (2020) Sonochemical synthesis and characterization

of silver tungstate nanostructures as visible-light-driven photocatalyst for waste-water treatment. Sep. Purif. Technol. 248: 117062-1-117062-11

17. E.K. Papynov, O.O. Shichalin, A.A. Belov, I.Y. Buravlev, A.S. Portnyagin, S.A. Azon, D.K. Shlyk, A.A. Buravleva, Y.A. Parot'kina, V.A. Nepomnyushchaya, Z.E. Kornakova, A.V. Gridasov, I.G. Tananaev, V.I. Sergienko, Synthesis of mineral-like SrWO₄ ceramics with the scheelite structure and a radioisotope product based on it. Russ J. Inorg. Chem. **66**, 1434–1446 (2021)

18. S. Raghunath, R. Balan, Solvent assisted synthesis and characterization of AMoO₄ (A = Ca, Sr & Ba) nanomaterials. Mater. Today Proc. **46**, 2930–2933 (2021)

19. F. Namvar, S.K. Abass, F. Soofivand, M. Salavati-Niasari, H. Moayedi, Sonochemical synthesis of Pr₆MoO₁₂ nanostructures as an effective photocatalyst for waste-water treatment. Ultrason. Sonochem. **58**, 1046871–0468712 (2019)

20. T. Kokulnathan, E.A. Kumar, T.J. Wang, I.C. Cheng, Electrochemical behavior of three-dimensional cobalt manganate with flowerlike structures for effective roxarsone sensing. Ecotoxicol. Environ. Saf. **208**, 17986–17996 (2021)

21. J.L. Silva Junior, F.X. Nobre, F.A. de Freitas, T.A.F. de Carvalho, S.S. de Barros, M.C. Nascimento, L. Manzato, J.M.E. Matos, W.R. Brito, Y. Leyet, P.R.C. Couceiro, Copper molybdate synthesized by sonochemistry route at room temperature as an efficient solid catalyst for esterification of oleic acid. Ultrason. Sonochem. **73**, 105541-1–105541-11 (2021)

22. A. Manickavasagan, R. Ramachandran, S.M. Chen, M. Velluchamy, Ultrasonic assisted fabrication of silver tungstate encrusted polypyrrole nanocomposite for effective photocatalytic and electrocatalytic applications. Ultrason. Sonochem. **64**, 104913-1–104913-13 (2020)

23. M. Sabaghi, Z. Aghajani, G.R. Najafi, Fabrication of a new heterogeneous tungstate-based on the amino-functionalized metal-organic framework as an efficient catalyst towards sonochemical oxidation of alcohols under green condition. J. Organomet. Chem. **925**, 121483-1–121483-9 (2020)

24. G. Harichandran, P. Divya, J. Yesuraj, B. Muthuraaman (2020) Sonochemical synthesis of chain-like ZnWO₄ nanoarchitectures for high performance supercapacitor electrode application. Mater. Charact. 167: 110490-1-110490-11

25. T. Kokulnathan, J.V. Kumar, S.M. Chen, R. Karthik, A. Elangovan, V. Muthuraj, One-step sonochemical synthesis of 1D β-stannous tungstate nanorods: an efficient and excellent electrocatalyst for the selective electrochemical detection of antipsychotic drug chlorpromazine. Ultrason. Sonochem. **44**, 231–239 (2018)

26. H.A. Sarode, D.P. Barai, B.A. Bhanvase, R.P. Ugwekar, V. Saharan, Investigation on preparation of graphene oxide-CuO nanocomposite based nanofluids with the aid of ultrasound assisted method for intensified heat transfer properties. Mater. Chem. Phys. **251**, 123102-1–123102-14 (2020)

27. P. Sundaresan, A. Yamuna, S.M. Chen, Sonochemical synthesis of samarium tungstate nanoparticles for the electrochemical detection of nilutamide. Ultrason. Sonochem. **67**, 105146 (2020)

28. A. Yamuna, P. Sundaresan, S. Chen, W. Shih, Ultrasound assisted synthesis of praseodymium tungstate nanoparticles for the electrochemical detection of cardioselective β-blocker drug. Microchem. J. **159**, 105420 (2020)

29. O. Rabbani, S. Ghasemi, S.R. Hosseini, Sonochemical assisted synthesis of manganese–nickel molybdate/reduced graphene oxide nanohybrid for energy storage. J. Alloys Compd. **840**, 15566 (2020)

30. L. Xu, S.H. Wang, Y. Jin, N.P. Liu, X.Q. Wu, X. Wang, Preparation of Cobalt tungstate nanomaterials and study on sonocatalytic degradation of Safranin t. Sep. Purif. Technol. **276**, 119405 (2021)

31. M. Pirsaheb, N. Moradi, A systematic review of the sonophotocatalytic process for the decolorization of dyes in aqueous solution: Synergistic mechanisms, degradation pathways, and process optimization. J. Water Process. Eng. **44**, 102314–1102314 (2021)

32. S.L. Liu, B. Liu, Z. Xiang, L. Xu, X.F. Wang, Y. Liu, X. Wang, Fabrication of CaWO₄ microspheres with enhanced sonocatalytic performance for ciprofloxacin removal in aqueous solution. Colloids Surf. Physicochem. Eng. Asp. **628**, 127206 (2021)

33. L. Xu, X.F. Wang, B. Liu, T. Sun, X. Wang, Sonocatalytic degradation of ciprofloxacin using hydrogel beads of TiO₂ incorporated biochar and chitosan. Colloids Surf. Physicochem. Eng. Asp. **627**, 127222 (2021)

34. S. Ahmadi, A. Rahdar, C.A. Igwegbe, S. Mortazavi-Derazkola, A.M. Banach, S. Rahdar, A.K. Singh, S. Rodriguez-Couto, G.Z. Kyzas, Praseodymium-doped cadmium tungstate (CdWO₄) nanoparticles for dye degradation with sonocatalytic process. Polyhedron **190**, 114792 (2020)

35. A.V. Karim, A. Shriwastav, Degradation of amoxicillin with sono, photo, and sonophotocatalytic oxidation under low-frequency ultrasound and visible light. Environ. Res. **200**, 111515 (2021)

36. N. Dirany, A. Hallaoui, J.C. Valmalette, M. Arab, Effect of morphology and temperature treatment control on the

1108 photocatalytic and photoluminescence properties of SrWO₄
1109 crystals. Photochem. Photobiol Sci. **19**, 235–250 (2020)

37. M. Kusuma, K.V. Jagannath, Solution combustion synthesis of SrMoO₄ nanophosphor using different molybdenum sources and study of its photocatalytic properties. Mater. Res. Express **6**, 1050a1 (2019)

38. B.K. Nirupama, Mandal, Visible-light active nanomaterials for environmental remediation—a mini review. Biointerface Res. Appl. Chem. **12**, 2535 (2022)

39. K. Prakruthi, M.P. Ujwal, S.R. Yashas, B. Mahesh, N.K. Swamy, H.P. Shivaraju, Recent advances in photocatalytic remediation of emerging organic pollutants using semiconducting metal oxides: an overview. Environ. Sci. Pollut. Res. **29**, 4930–4957 (2022)

40. P.B. de Sousa, I.C. Nogueira, J.C. Sczancoski, B.C. Viana, M.R.M.C. Santos, E. Longo, L.S. Cavalcante, Structural refinement, morphological features and optical, photo- and sonophotocatalytic properties of (Ca₁₋ₓSrₓ)WO₄ synthesized by the sonochemical method. J. Photocatal. **2**, 147–164 (2021)

41. H.M. Rietveld, A profile refinement method for nuclear and magnetic structures J. Appl. Crystallogr. **2**, 65–71 (1969)

42. A.C. Larson, R.B. Von Dreele, *General Structure Analysis System (GSAS)* (Los Alamos National Laboratory Report LAUR 86–748, New Mexico, USA, 2004)

43. L.W. Finger, D.E. Cox, A.P. Jephcoat, A correction for powder diffraction peak asymmetry due to axial divergence. J. Appl. Crystallogr. **27**, 892–900 (1994)

44. P.W. Stephens, Phenomenological model of anisotropic peak broadening in powder diffraction. J. Appl. Crystallogr. **32**, 281–289 (1999)

45. K. Momma, F. Izumi, VESTA: a three-dimensional visualization system for electronic and structural analysis. J. Appl. Crystallogr. **41**, 653–658 (2008)

46. K. Momma, F. Izumi, VESTA 3 for three-dimensional visualization of crystal, volumetric and morphology data. J. Appl. Crystallogr. **44**, 1272–1276 (2011)

47. I.C. Nogueira, L.S. Cavalcante, P.F.S. Pereira, M.M. de Jesus, J.M. Rivas Mercury, N.C. Batista, M.S. Li, E. Longo, Rietveld refinement, morphology and optical properties of (Ba₁₋ₓSrₓ) MoO₄ crystals. J. Appl. Crystallogr. **46**, 1434–1446 (2013)

48. S.P. Culver, M.J. Greaney, A. Tinoco, R.L. Brutchey, Low-temperature synthesis of homogeneous solid solutions of scheelite-structured Ca₁₋ₓSrₓWO₄ and Sr₁₋ₓBaₓWO₄ nanocrystals. Dalt Trans. **44**, 15042–15048 (2015)

49. W. Li, A. Gurlo, R. Riedel, E. Ionescu, Perovskite-type solid solution SrMo₁₋ₓWₓ(O,N)₃ oxynitrides: synthesis, structure, and magnetic properties. Z. Anorg. Allg. Chem. **641**, 1533–1539 (2015)

50. S.H. Lee, L.K. Bharat, J.S. Yu, Enhanced luminescent properties in Eu³⁺-activated SrMoₓW₁₋ₓO₄ red-emitting phosphors for solid-state lighting and field-emission displays. J. Alloys Compd. **726**, 698–706 (2017)

51. J. Zhang, R. Li, L. Liu, L. Li, S. Zou, G. Gan, G. Ji, Self-assembled 3D sphere-like SrMoO₄ and SrMoO₄: Ln³⁺ (Ln = Eu, Sm, Tb, Dy) microarchitectures: facile sonochemical synthesis and optical properties. Ultrason. Sonochem. **21**, 1736–1744 (2014)

52. H. Gao, C. Yu, Y. Wang, S. Wang, H. Yang, F. Wang, S. Tang, Z. Yi, D. Li, A novel photoluminescence phenomenon in a SrMoO₄/SrWO₄ micro/nano heterojunction phosphors obtained by the polyacrylamide gel method combined with low temperature calcination technology. J. Lumin. **243**, 118660 (2011)

53. D. Das, S.K. Gupta, A.P. Srivastava, P. Utpalla, K. Sudarshan, Probing emission and defects in BaWₓMo₁₋ₓO₄ solid solutions: achieving color tunable luminescence by W/Mo ratio and size manipulation. New. J. Chem. **44**, 10380–10389 (2020)

54. M.C. Oliveira, J. Andrés, L. Gracia, M.S.M.P. de Oliveira, J.M.R. Mercury, E. Longo, I.C. Nogueira, Geometry, electronic structure, morphology, and photoluminescence emissions of BaW₁₋ₓMoₓO₄ (x = 0, 0.25, 0.50, 0.75, and 1) solid solutions: theory and experiment in concert. Appl. Surf. Sci. **463**, 907–917 (2019)

55. M. Muralidharan, V. Anbarasu, A.E. Perumal, K. Sivakumar, Enhanced ferromagnetism in Cr doped SrMoO₄ scheelite structured compounds. J. Mater. Sci. Mater. Electron. **27**, 2545–2556 (2016)

56. D.F. Dos Santos, L.X. Lovisa, A.A.G. Santiago, M.S. Li, E. Longo, M.R.D. Bomio, F.V. Motta, Growth mechanism and vibrational and optical properties of SrMoO₄:Tb³⁺, Sm³⁺ particles: green–orange tunable color. J. Mater. Sci. **55**, 8610–8629 (2020)

57. T. Thongtem, S. Kungwankunakorn, B. Kuntalue, A. Phuruangrat, S. Thongtem, Luminescence and absorbance of highly crystalline CaMoO₄, SrMoO₄, CaWO₄ and SrWO₄ nanoparticles synthesized by co-precipitation method at room temperature. J. Alloys Compd. **506**, 475–481 (2010)

58. T.T. Basiev, A.A. Sobol, Y.K. Voronko, P.G. Zverev, Spontaneous Raman spectroscopy of tungstate and molybdate crystals for Raman lasers. Opt. Mater. **15**, 205–216 (2000)

59. A. Shandilya, K. Sreenivas, Microstructural and thermogravimetric analysis of SrMoO4 prepared by solid state reaction. AIP Conf. Proc. **2142**, 070028 (2019)

60. J. Suda, P.G. Zverev, Investigation of band gap effect and dephasing on Raman line broadening for the highest-

frequency Ag mode in comparison with SrWO$_4$ and SrMoO$_4$. Vib. Spectrosc. **84**, 127–132 (2016)

61. J.C. Sczancoski, W. Avansi, M.G.S. Costa, M.S. Li, V.R. Mastelaro, R.S. Santos, E. Longo, L.S. Cavalcante, Effect of different strontium precursors on the growth process and optical properties of SrWO$_4$ microcrystals. J. Mater. Sci. **50**, 8089–8103 (2015)

62. S.P. Culver, F.A. Rabuffetti, S. Zhou, M. Mecklenburg, Y. Song, B.C. Melot, R.L. Brutchey, Low-temperature synthesis of AMoO$_4$ (A = Ca, Sr, Ba) scheelite nanocrystals. Chem. Mater. **25**, 4129–4134 (2013)

63. V. Chauhan, P. Dixit, P.C. Pandey, Bi^{3+} assisted luminescence in SrMoO$_4$:Sm^{3+} red phosphors. J. Rare Earths **39**, 1336–1343 (2021)

64. T. Thongtem, A. Phuruangrat, S. Thongtem, Microwave-assisted synthesis and characterization of SrMoO$_4$ and SrWO$_4$ nanocrystals. J. Nanoparticle Res. **12**, 2287–2294 (2010)

65. Y. Wang, J. Wang, L. Geng, H. Wang, J. Cao, S. Chen, Successful synthesis of single scheelite-structured CdW$_{1-x}$Mo$_x$O$_4$ continuous solid-solution and its composition-dependent optoelectronic properties. J. Solid State Chem. **266**, 74–82 (2018)

66. M. Daturi, L. Savary, G. Costentin, J.C. Lavalley, A correlation between crystal structure and catalytic activity in the solid solutions CdMo$_x$W$_{1-x}$O$_4$. Catal. Today **61**, 231–236 (2000)

67. J.C. Rendón-Angeles, Z. Matamoros-Veloza, L.A. Gonzalez, J. López-Cuevas, T. Ueda, K. Yanagisawa, I. Hernández-Calderón, M. Garcia-Rocha, Rapid hydrothermal synthesis of SrMo$_{1-x}$W$_x$O$_4$ powders: structure and luminescence characterization. Adv. Powder Technol. **28**, 629–640 (2017)

68. W. Jiang, W. Zhu, C. Peng, F. Yang, S. Xuan, X. Gong, Controllable synthesis of hierarchical strontium molybdate by sonochemical method. Cryst. Res. Technol. **47**, 997–1003 (2012)

69. J. Mukherjee, D.P. Dutta, J. Ramakumar, A.K. Tyagi, A comprehensive study on the uptake of dyes, Cu(II) and radioactive ^{137}Cs$^{(I)}$ by sonochemically synthesized strontium/yttrium tungstate and molybdate nanoparticles. J. Environ. Chem. Eng. **4**, 3050–3064 (2016)

70. L.S. Cavalcante, J.C. Sczancoski, N.C. Batista, E. Longo, J.A. Varela, M.O. Orlandi, Growth mechanism and photocatalytic properties of SrWO4 microcrystals synthesized by injection of ions into a hot aqueous solution. Adv. Powder Technol. **24**, 344–353 (2013)

71. P. Kubelka, F. Munk, Ein Beitrag Zur Optik Der Farbanstriche. Z. Techn. Phys. **12**, 593–601 (1931)

72. V.M. Longo, E. Orhan, L.S. Cavalcante, S.L. Porto, J.W.M. Espinosa, J.A. Varela, E. Longo, Understanding the origin of photoluminescence in disordered Ca$_{0.60}$Sr$_{0.40}$WO$_4$: an experimental and first-principles study. Chem. Phys. **334**, 180–188 (2007)

73. M. Muralidharan, K. Sivaji, Vacancy induced ferromagnetism in SrWO4 and SrMoO4 nano structured compounds. AIP Conf. Proc. **2265**, 030584 (2020)

74. Y. Wang, H. Xu, C. Shao, J. Cao, Doping induced grain size reduction and photocatalytic performance enhancement of SrMoO$_4$: Bi^{3+}. Appl. Surf. Sci. **392**, 649–657 (2017)

75. N. Khobragade, E. Sinha, S.K. Rout, M. Kar, Structural, optical and microwave dielectric properties of Sr$_{1-x}$Ca$_x$WO$_4$ ceramics prepared by the solid state reaction route. Ceram. Int. **39**, 9627 (2013)

76. S.K. Gupta, K. Sudarshan, P.S. Ghosh, K. Sanyal, A.P. Srivastava, A. Arya, P.K. Pujari, R.M. Kadam, Eu^{3+} local site analysis and emission characteristics of novel Nd$_2$Zr$_2$O$_7$:Eu phosphor: insight into the effect of europium concentration on its photoluminescence properties. RSC Adv. **6**, 53614–53624 (2016)

77. F.D. Fedyunin, D.A. Spassky, Urbach rule and estimation of the energy gap width in molybdates. Phys. Solid State **62**, 1325–1332 (2020)

78. L. Li, Y. Pan, W. Chang, Z. Feng, P. Chen, C. Li, Z. Zeng, X. Zhou, Near-infrared downconversion luminescence of SrMoO$_4$: Tm^{3+}, Yb^{3+} phosphors. Mater. Res. Bull. **93**, 144–149 (2017)

79. D. Errandonea, L. Gracia, R. Lacomba-Perales, A. Polian, J.C. Chervin, Compression of scheelite-type SrMoO$_4$ under quasi-hydrostatic conditions: redefining the high-pressure structural sequence. J. Appl. Phys. **113**, 123510 (2013)

80. I.P. Carvalho, A.F. Lima, M.V. Lalic, Theoretical study of electronic and optical properties of the scheelite MWO$_4$ (M = Ca, Sr or Ba) compounds by applying the modified Becke-Johnson exchange-correlation potential. Opt. Mater. **92**, 187–194 (2019)

81. H. Gueffaf, B. Lagoun, A. Guibadj, S. Maabed, A. Gueddouh, DFT investigation of structural, electronic, elastic and optical properties of SrMO$_4$ (M = Mo and W). Commun. Theor. Phys. **68**, 536 (2017)

82. D.W. Kim, I.S. Cho, S.S. Shin, S. Lee, T.H. Noh, D.H. Kim, H.S. Jung, K.S. Hong, Electronic band structures and photovoltaic properties of MWO$_4$ (M = Zn, Mg, Ca, Sr) compounds. J. Solid State Chem. **184**, 2103–2107 (2011)

83. R. Lacomba-Perales, D. Errandonea, A. Segura, J. Ruiz-Fuertes, P. Rodríguez-Hernández, S. Radescu, J. López-Solano, A. Mujica, A. Muñoz, A combined high-pressure experimental and theoretical study of the electronic band-

structure of scheelite-type AWO₄ (A = Ca, Sr, Ba, Pb) compounds. J. Appl. Phys. **110**, 043703 (2011)

84. D.B. Miklos, C. Remy, M. Jekel, K.G. Linden, J.E. Drewes, U. Hübner, Evaluation of advanced oxidation processes for water and wastewater treatment–a critical review. Water Res. **139**, 118–131 (2018)

85. P. Sathishkumar, R.V. Mangalaraja, S. Anandan, Review on the recent improvements in sonochemical and combined sonochemical oxidation processes–a powerful tool for destruction of environmental contaminants. Renew. Sustain. Energy Rev. **55**, 426–454 (2016)

86. G. Fan, S. Yang, B. Du, J. Luo, X. Lin, X. Li, Sono-photo hybrid process for the synergistic degradation of levofloxacin by FeVO₄/BiVO₄: Mechanisms and kinetics. Environ. Res. **204**, 112032 (2022)

87. A.A. Zewde, L. Zhang, Z. Li, E.A. Odey, A review of the application of sonophotocatalytic process based on advanced oxidation process for degrading organic dye. Rev. Environ. Health **34**, 365–375 (2019)

88. D. Panda, S. Manickam, Recent advancements in the sonophotocatalysis (SPC) and doped-sonophotocatalysis (DSPC) for the treatment of recalcitrant hazardous organic water pollutants. Ultrason. Sonochem **36**, 481–496 (2017)

89. R.A. Torres, J.I. Nieto, E. Combet, C. Pétrier, C. Pulgarin, Influence of TiO₂ concentration on the synergistic effect between photocatalysis and high-frequency ultrasound for organic pollutant mineralization in water. Appl. Catal. B Environ. **80**, 168–175 (2008)

90. L. Xu, X. Wang, M.L. Xu, B. Liu, X.F. Wang, S.H. Wang, T. Sun, Preparation of zinc tungstate nanomaterial and its sonocatalytic degradation of meloxicam as a novel sonocatalyst in aqueous solution. Ultrason. Sonochem **61**, 104815 (2020)

91. H. Ogi, M. Hirao, M. Shimoyama, Activation of TiO₂ photocatalyst by single-bubble sonoluminescence for water treatment. Ultrasonics **40**, 649 (2002)

92. H. Anwer, A. Mahmood, J. Lee, K.H. Kim, J.W. Park, A.C.K. Yip, Photocatalysts for degradation of dyes in industrial effluents: Opportunities and challenges. Nano Res. **12**, 955 (2019)

93. R.A. Roca, J.C. Sczancoski, I.C. Nogueira, M.T. Fabbro, H.C. Alves, L. Gracia, L.P.S. Santos, C.P. De Sousa, J. Andrés, G.E. Luz, E. Longo, L.S. Cavalcante, Facet-dependent photocatalytic and antibacterial properties of α-Ag₂WO₄ crystals: combining experimental data and theoretical insights. Catal. Sci. Technol. **5**, 4091–4107 (2015)

94. X. Chen, Z. Xue, Y. Yao, W. Wang, F. Zhu, C. Hong, Oxidation degradation of rhodamine b in aqueous by UV/S₂O₈ treatment system. Int. J. Photoenergy, **2012**, 754691-1–754691-5 (2012)

95. J. Bi, L. Wu, Y. Zhang, Z. Li, J. Li, X. Fu, Solvothermal preparation, electronic structure and photocatalytic properties of PbMoO₄ and SrMoO₄. Appl. Catal. B Environ. **91**, 135–143 (2009)

96. S.M. Hosseinpour-Mashkani, A. Sobhani-Nasab, M. Mehrzad, Controlling the synthesis SrMoO₄ nanostructures and investigation its photocatalyst application. J. Mater. Sci. Mater. Electron. **27**, 5758–5763 (2016)

97. R. Karthik, N. Karikalan, S.M. Chen, J.V. Kumar, C. Karuppiah, V. Muthuraj, Assessment of divergent functional properties of seed-like strontium molybdate for the photocatalysis and electrocatalysis of the postharvest scald inhibitor diphenylamine. J. Catal. **352**, 606–616 (2017)

98. M. Rahimi-Nasrabadi, Strontium molybdate nanostructures: synthesis of different shapes through a new approach and its photocatalyst application. J. Mater. Sci. Mater. Electron. **28**, 2200–2205 (2017)

99. Y. Zhu, G. Zheng, Z. Dai, L. Zhang, Y. Ma, Photocatalytic and luminescent properties of SrMoO₄ phosphors prepared via hydrothermal method with different stirring speeds. J. Mater. Sci. Technol. **33**, 23–29 (2017)

100. Y.N. Zhu, G.H. Zheng, Z.X. Dai, J.J. Mu, Z.F. Yao, Monodisperse SrMoO₄ nanocrystals: synthesis, luminescence and photocatalysis. J. Mater. Sci. Technol. **33**, 834–842 (2017)

101. A.M. Huerta-Flores, I. Juárez-Ramírez, L.M. Torres-Martínez, J.E. Carrera-Crespo, T. Gómez-Bustamante, O. Sarabia-Ramos, Synthesis of AMoO₄ (A = Ca, Sr, Ba) photocatalysts and their potential application for hydrogen evolution and the degradation of tetracycline in water. J. Photochem. Photobiol. A Chem. **356**, 29 (2018)

102. Y.L. Liu, Z.X. Dai, Z.F. Yao, G.H. Zheng, Y.Q. Ma, The photocatalytic performance for Mn-doping SrMoO₄ reduced in H₂/N₂ mixture atmospheres. Appl. Organomet. Chem. **34**, e5745-1–18 (2020)

103. Z.A. Mikhaylovskaya, E.S. Buyanova, S.A. Petrova, Y.A. Kuznetsova, D.V. Piankova, Synthesis and properties of (Ca/Sr)₁₋₃ₓBi₂ₓMoO₄ solid solutions. Inorg. Mater. **55**, 1020–1025 (2019)

104. S.P. Wang, Z.F. Yao, L.Y. Zhang, L. Yun, Y.L. Liu, Z.X. Dai, G.H. Zheng, Enhanced photocatalytic activity of SrMoO₄ via SrMo(O,N)₃ formation by annealing in NH₃ atmosphere. J. Electron. Mater. **48**, 6617 (2019)

105. L.Y. Zhang, G.H. Zheng, Z.X. Dai, X.D. Zhao, Synthesis of Co doping SrMoO₄ for enhanced photocatalytic performance via hydrothermal method. Dig. J. Nanomater. Biostruct. **14**, 569–579 (2019)

106. Y. Zhang, X. Yang, P. Zhang, D. Liu, Y. Wang, Z. Jin, B.B. Mamba, A.T. Kuvarega, J. Gui, One-step hydrothermal fabrication of SrMoO₄/MoS₂ composites with strong

interfacial contacts for efficient photoreduction removal of Cr(vi). CrystEngComm. **22**, 4489–4499 (2020)

107. L.Y. Zhang, A.B. Zhang, G.H. Zheng, Z.X. Dai, W. Yang, Synthesis of Cr-doped $SrMoO_4$ with enhanced photocatalytic performance via hydrothermal method. Dig. J. Nanomater. Biostruct. **16**, 283–296 (2021)

Publisher's Note Springer Nature remains neutral with regard to jurisdictional claims in published maps and institutional affiliations.